



Sedimentology, chemostratigraphy, and stromatolites of lower Paleoproterozoic carbonates, Turee Creek Group, Western Australia

Citation

Martindale, Rowan C., Justin V. Strauss, Erik A. Sperling, Jena E. Johnson, Martin J. Van Kranendonk, David Flannery, Katherine French, et al. 2015. "Sedimentology, Chemostratigraphy, and Stromatolites of Lower Paleoproterozoic Carbonates, Turee Creek Group, Western Australia." *Precambrian Research* 266 (September): 194–211. doi:10.1016/j.precamres.2015.05.021.

Published Version

doi:10.1016/j.precamres.2015.05.021

Permanent link

<http://nrs.harvard.edu/urn-3:HUL.InstRepos:27727027>

Terms of Use

This article was downloaded from Harvard University's DASH repository, and is made available under the terms and conditions applicable to Open Access Policy Articles, as set forth at <http://nrs.harvard.edu/urn-3:HUL.InstRepos:dash.current.terms-of-use#OAP>

Share Your Story

The Harvard community has made this article openly available.
Please share how this access benefits you. [Submit a story](#).

[Accessibility](#)

1 **Sedimentology, chemostratigraphy, and stromatolites of lower Paleoproterozoic**
2 **carbonates, Turee Creek Group, Western Australia**

3

4 Rowan C. Martindale ^{a, b, *}, Justin V. Strauss ^c, Erik A. Sperling ^c, Jena E. Johnson ^d,
5 Martin J. Van Kranendonk ^e, David Flannery ^{f, g}, Katherine French ^h, Kevin Lepot ⁱ, Rajat
6 Mazumder ^j, Melissa S. Rice ^{d, k}, Daniel P. Schrag ^c, Roger Summons ^h, Malcolm Walter
7 ^f, John Abelson ^l, Andrew H. Knoll ^{a, c}

8

9 ^a Department of Organismic and Evolutionary Biology, Harvard University, 26 Oxford
10 Street, Cambridge, Massachusetts, USA, 02138

11 ^b Department of Geological Sciences, University of Texas at Austin, 1 University Station
12 C1100, Austin, Texas, USA, 78712

13 ^c Department of Earth and Planetary Sciences, Harvard University, 20 Oxford Street,
14 Cambridge, Massachusetts, USA 02138

15 ^d Division of Geological and Planetary Sciences, California Institute of Technology, 1200
16 E California Blvd, Pasadena CA 91125

17 ^e Australian Centre for Astrobiology and School of Biological Earth and Environmental
18 Sciences, University of New South Wales Australia, Kensington, NSW 2052 Australia

19 ^f Australian Centre for Astrobiology and School of Biotechnology and Biomolecular
20 Sciences, University of New South Wales Australia, Kensington, NSW 2052 Australia

21 ^g Jet Propulsion Laboratory, California Institute of Technology, 1200 E California Blvd,
22 Pasadena CA 91125

23 ^h Department of Earth, Atmospheric, and Planetary Sciences; Massachusetts Institute of
24 Technology, Cambridge, MA 02139, USA.

25 ⁱ Laboratoire d'Océanologie et de Géosciences, Université de Lille, CNRS UMR8187,
26 59655 Villeneuve d'Ascq, France.

27 ^j Department of Applied Geology, Faculty of Engineering and Science, Curtin University
28 Sarawak, CDT 250, 98009 Miri, Sarawak, Malaysia.

29 ^k Melissa S. Rice, Geology Department, Western Washington University, 516 High
30 Street, MS 9080, Bellingham, WA 98225

31 ^l The Agouron Institute, Pasadena, CA 91106, USA

32

33 *Corresponding author

34 *e-mail address: Martindale@jsg.utexas.edu*

35 *Telephone Number: 1-512-475-6439*

36 *Address: 1 University Station C1100*

37 *Austin, TX, USA, 78712*

38

39 ABSTRACT

40 The ca. 2.45–2.22 Ga Turee Creek Group, Western Australia, contains carbonate-
41 rich horizons that postdate earliest Proterozoic iron formations, bracket both
42 Paleoproterozoic glaciogenic beds and the onset of the Great Oxidation Event (GOE),
43 and predate ca. 2.2–2.05 Ga Lomagundi-Jatuli C-isotopic excursion(s). As such, Turee
44 Creek carbonate strata provide an opportunity to characterize early Paleoproterozoic
45 carbonate sedimentation and carbon cycle dynamics in the context of significant global
46 change. Here, we report on the stratigraphy, sedimentology, petrology, carbon isotope
47 chemostratigraphy, and stromatolite development for carbonate-rich successions within
48 the pre-glacial part of the Kungarra Formation and the postglacial Kazput Formation.

49 Kungarra carbonate units largely occur as laterally discontinuous beds within a
50 thick, predominantly siliciclastic shelf deposit. While this succession contains thin
51 microbialite horizons, most carbonates consist of patchy calcite overgrowths within a
52 siliciclastic matrix. C-isotopic values show marked variation along a single horizon and
53 even within hand samples, reflecting spatially and temporally variable mixing between
54 dissolved inorganic carbon in seawater and isotopically light inorganic carbon generated
55 via syn- and post-depositional remineralization of organic matter.

56 In contrast, the Kazput carbonates consist of subtidal stromatolites, grainstones,
57 and micrites deposited on a mixed carbonate-siliciclastic shelf. These carbonates exhibit
58 moderate $\delta^{13}\text{C}$ values of -2‰ to +1.5‰ and likely preserve a C-isotopic signature of
59 seawater. Kazput carbonates, thus, provide some of the best available evidence that an
60 interval of unexceptional C-isotopic values separates the Lomagundi-Jatuli C-isotopic
61 excursion(s) from the initiation of the GOE as inferred from multiple sulfur isotopes (loss

62 of mass independent fractionation). The Kazput Formation also contains unusual, m-scale
63 stromatolitic buildups, which are composed of sub-mm laminae and discontinuous,
64 convex upward lenticular precipitates up to a few mm in maximum thickness. Laminae,
65 interpreted as microbial mat layers, contain quartz and clay minerals as well as calcite,
66 whereas precipitate lenses consist of interlocking calcite anhedral, sometimes showing
67 faint mm-scale banding. These cements formed either as infillings of primary voids
68 formed by gas emission within penecontemporaneously lithified mats, or as local seafloor
69 precipitates that formed on, or within, surface mats. It is possible that both mechanisms
70 interacted to form the unique Kazput stromatolites. These microbialites speak to a
71 distinctive interaction between life and environment early in the Paleoproterozoic Era.

72

73 *Keywords: Turee Creek Group; Kazput Formation; Kungarra Formation; Great*
74 *Oxidation Event; stromatolite; Lomagundi-Jatuli Event.*

75

76 **1. Introduction**

77 Lower Paleoproterozoic sedimentary rocks record a number of first-order changes
78 in the Earth system, including globally extensive ice sheets, one or more extreme states of
79 the carbon cycle characterized by uniquely high $\delta^{13}\text{C}$ in carbonates, and the initial
80 accumulation of oxygen in the atmosphere and surface oceans (Akin et al., 2013; Asael et
81 al., 2013; Bekker and Holland, 2012; Bekker et al., 2004, 2013; Farquhar et al., 2000;
82 Fralick et al., 2011; Hoffman, 2013; Konhauser et al., 2011; Lyons et al., 2012, 2014;
83 Melezhik and Fallick, 2010; Partin et al., 2013; Planavsky et al., 2012, 2014; Pufahl and
84 Hiatt, 2012; Pufahl et al., 2010, 2011; Reinhard et al., 2013; Scott et al., 2014; Swanner et

85 al., 2014; and references therein). Co-occurring global glaciation, carbon isotopic
86 variation, and redox change also characterize Neoproterozoic rocks, and for this younger
87 interval, carbonate strata have played an important role in both recording key events and
88 providing context for the interpretation of these events (e.g., Halverson and Shields-Zhou,
89 2011; Johnston et al., 2012). Detailed analyses of platform and shelf carbonates are
90 available for Neoproterozoic successions [e.g., the Campbellrand/Malmani subgroups of the
91 Transvaal Supergroup, South Africa; (Knoll and Beukes, 2009; and references therein)]
92 and younger Paleoproterozoic rocks [e.g., 2 Ga platform carbonates of the Slave
93 Province, Canada; (Hotinski et al., 2004)]. To date, however, relatively few studies have
94 focused on lower Paleoproterozoic carbonates, despite their potential importance in
95 understanding early Paleoproterozoic evolution and environmental change.

96 The ca. 2.45–2.22 Ga Turee Creek Group, exposed in the Hamersley Range of
97 Western Australia, conformably overlies earliest Paleoproterozoic iron formations,
98 predates the ca. 2.2 Ga onset of the Lomagundi-Jatuli C-isotopic excursion(s), and hosts
99 carbonate and glacially-influenced strata that record onset of the Great Oxidation Event
100 (GOE) (Bekker et al., 2004; Martin et al., 2013; Van Kranendonk and Mazumder, 2015).
101 Thus, these carbonates provide an opportunity to characterize the response of early
102 Paleoproterozoic carbonate deposition and carbon cycle dynamics to significant global
103 change, including the GOE and glaciation. Here, we report on the stratigraphy,
104 sedimentology, carbonate petrology, carbon isotope chemostratigraphy, and stromatolite
105 development in two closely spaced sections of the Kazput Formation of the upper Turee
106 Creek Group. We also report lithological and isotopic data from three parallel
107 stratigraphic sections from the older Kungarra Formation of the lower Turee Creek

108 Group. Together, these data place carbonate strata of the Turee Creek Group in the
109 context of profound global change following the early oxygenation of Earth's surface
110 environments.

111

112 **2. Geologic Setting**

113 The Turee Creek Group of the Mount Bruce Supergroup is the youngest
114 sedimentary succession within the Hamersley Basin of the Pilbara Craton (Trendall,
115 1990). Turee Creek Group rocks conformably overlie iron formations of the Hamersley
116 Group and sit unconformably beneath sedimentary and volcanic deposits of the Wyloo
117 Group (Fig. 1) (Horwitz, 1982; Thorne, 1990; Thorne and Seymour, 1991; Trendall,
118 1969; Trendall et al., 1983). Initial research suggested conformable relationships
119 throughout the Proterozoic stratigraphy of Western Australia (e.g., Trendall and
120 Blockley, 1970), but continuing stratigraphic and geochronological studies have since
121 identified significant unconformities and deformational events that point to a protracted,
122 but episodic, depositional history spanning more than 330 Myr (Martin et al., 2000; and
123 references therein).

124 Palinspastic reconstructions and basin analysis of upper Hamersley Basin and
125 lower Wyloo Group stratigraphy led Horwitz (1982) to propose a post-Hamersley
126 depositional feature, called the McGrath Trough, that reflects flexural subsidence driven
127 by peripheral or retroarc foreland basin development (Horwitz, 1982; Krapež, 1996;
128 Martin, 1999; Martin et al., 2000; Powell and Horwitz, 1994). The foreland-related
129 tectonostratigraphic sequence most likely involves the Turee Creek and lower Wyloo
130 groups (Martin et al., 2000); however, some authors have argued that it only involves the

131 Turee Creek Group (e.g., Blake and Barley, 1992; Krapež, 1996) or both the Turee Creek
132 and entire Wyloo groups (e.g., Thorne and Seymour, 1991; Tyler and Thorne, 1990).
133 More recently, Van Kranendonk et al. (2015) suggested the Turee Creek Group was
134 deposited in an intracratonic basin. Regardless of McGrath dynamics, the 3–4 km thick
135 Turee Creek Group records rapid lateral facies change (e.g., Martin et al., 2000 and
136 references therein).

137 The Turee Creek Group consists, in stratigraphic order, of the Kungarra
138 (including the glaciogenic Meteorite Bore Member), Koolbye, and Kazput formations
139 (Fig. 1) (Thorne et al., 1995; Trendall, 1979, 1981). It is bracketed in age by the 2449 ± 3
140 Ma Woongarra Rhyolite (Barley et al., 1997) near the top of the underlying Hamersley
141 Group and the 2209 ± 15 Ma Cheela Springs Basalt (Martin et al., 1998) low in the
142 unconformably overlying Wyloo Group succession (Fig. 1). Müller et al. (2005)
143 reinterpreted the Cheela Springs date as a reflection of provenance rather than
144 crystallization age, but their U-Pb age on baddeleyite of 2208 ± 15 Ma for diorite sills
145 that cut the Turee Creek Group provides an essentially indistinguishable maximum age
146 constraint. The Kungarra Formation of the Turee Creek Group is further constrained to be
147 younger than ca. 2420 Ma, based on U-Pb ages of detrital zircons in the Meteorite Bore
148 Member (Takehara et al., 2010). Turee Creek Group strata record a broad shallowing-
149 upward profile from deep-water banded iron formation (the Boolgeeda Iron Formation of
150 the underlying Hamersley Group), through fine-grained siliciclastic deposits of the
151 Kungarra Formation, to fluvial and shallow marine strata of the Koolbye and Kazput
152 formations.

153 Although detailed correlation with other Paleoproterozoic successions is
154 challenging, Turee Creek Group strata record two events that guide interbasinal
155 correlation. First, Williford et al. (2011) documented mass independent sulfur isotope
156 fractionation, a proxy for the near-absence of environmental oxygen (Farquhar et al.,
157 2000), in the lower part of the Meteorite Bore Member of the Kungarra Formation. On
158 this basis, the authors suggested that the lower glaciogenic unit of the Meteorite Bore
159 Member, locally in contact with the Boolgeeda Iron Formation, was deposited during the
160 final stages of the GOE, when oxygen levels were still low enough for the development
161 of MIF-S, but sufficiently high for oxidative weathering of continental sulfides and
162 significant sulfur isotope fractionation.

163 The glacial character of the Meteorite Bore Member and a second recently
164 discovered unit of glacial diamictite in the Kungarra Formation provide a means of
165 correlation to other Paleoproterozoic basins (Martin, 1999; Trendall, 1976; Van
166 Kranendonk and Mazumder, 2015). Martin (1999) and Van Kranendonk et al. (2012)
167 pointed to analogous basin histories of the South African Transvaal Supergroup and the
168 Canadian Huronian Supergroup on the basis of similar ca. 2.45 Ga felsic magmatic
169 events followed by glacial episodes and mafic magmatism at ca. 2.2 Ga. Hoffman (2013)
170 suggested a similar global correlation scheme based on the assumption that the GOE, as
171 marked by the disappearance of MIF-S, was a unique event connected in time to a
172 Snowball Earth event (Kirschvink et al., 2000). By this reasoning, disparate sedimentary
173 rocks may be correlated by a single tie point, even though some regions record three
174 glacial events and others only record two. Thus, while it is difficult to assign an exact age
175 to the Turee Creek Group, the glacial history of these strata generally enables broad

176 correlation to the timing of the Great Oxidation Event (Van Kranendonk and Mazumder,
177 2015).

178

179 **3. Methods**

180 Fieldwork for this project was conducted as part of the 2012 Advanced
181 Geobiology Course sponsored by the Agouron Institute. Five stratigraphic sections were
182 measured and sampled from three sites in the Hardey Syncline: the Horseshoe Creek
183 locality of Lindsay and Brasier (2002) (Fig. 1, three sections at site 1) and two Kazput
184 Formation localities, K1 and K2, on the southwest and northeast limbs of a small NNW-
185 SSE-trending anticline in the central part of the Syncline (Fig. 1, sites 2 and 3). The
186 Horseshoe Creek strata were previously described by Lindsay and Brasier (2002) as
187 Kazput Formation, but regional mapping places this section below the Meteorite Bore
188 Member and is thus part of the Kungarra Formation (Fig. 1) (Martin et al., 2000; Van
189 Kranendonk, 2010; Van Kranendonk et al., 2015).

190 At Horseshoe Creek, three parallel stratigraphic columns were measured through
191 ~120 m of the Kungarra Formation to determine patterns of lateral facies change and
192 geochemical variation (HC1, HC2, and HC3). The first Kazput section was measured
193 through roughly 140 m of sedimentary rocks on the west-southwestern limb of the
194 anticline (locality K1), and the second section is a composite stratigraphic column
195 measured across two ridges (roughly 100 m apart) on the southwestern limb of the
196 anticline (localities K2A, K2B, and K2C). Although the K1 and K2 localities are within a
197 few kilometers of each other, their exact correlation is uncertain due to differing facies
198 development and structural complications.

199 Rock samples were collected from each measured section at roughly 1–3 m
200 intervals for geochemical and petrological analysis; samples were cut using a diamond
201 saw, and made into thin sections for petrographic analysis. Thin section blanks were then
202 microdrilled following methods of Kaufman et al. (1990) to obtain fresh powder. Blanks
203 were commonly drilled several times if multiple lithologies or microfacies were present
204 in a single thin section.

205 Carbonate $\delta^{13}\text{C}$ and $\delta^{18}\text{O}$ values for 225 Kazput and 125 Kungarra samples were
206 measured on a VG Optima dual inlet mass spectrometer fed by an Isocarb preparation
207 device in the Harvard University Laboratory for Geochemical Oceanography (see
208 supplementary data). Approximately 1 mg of carbonate powder was dissolved in a
209 common anhydrous phosphoric acid (H_3PO_4) bath kept at 90°C for eight minutes. Carbon
210 dioxide gas was purified cryogenically and measured against an in-house reference gas.
211 No dolomite corrections were applied to the data. Analytical uncertainty was $\pm 0.1\%$
212 (sample:standard ratio of 8:1); results are reported on a Vienna Pee Dee Belemnite scale.

213 Two samples were additionally analyzed using a scanning electron microscope
214 (SEM) with an attached electron dispersive spectrometer (EDS). These small-scale
215 analyses are employed to visualize and compare textures of the two carbonates, as well as
216 to provide a high-resolution map of the stromatolitic laminae from the Kazput Formation.
217 A representative sample from the Kungarra Formation (from 16.25 m in section HC3)
218 and a stromatolite from the Kazput Formation (KAZS1), were photographed using
219 backscatter detector imaging to highlight compositional contrasts on a Zeiss 1550VP
220 Field Emission SEM in the California Institute of Technology Geological and Planetary
221 Sciences Division Analytical Facility. An Oxford INCA Energy 300 EDS system was

222 utilized to produce elemental color maps of key elements [Si, Ca, C, Fe, Al, Mg] and
223 these maps were superimposed on backscatter images to highlight different minerals.
224 Elemental analyses have relative accuracy of better than 5%.

225

226 **4. Results: Sedimentology, facies analysis, and petrography**

227 *4.1. Kungarra Formation at Horseshoe Creek*

228 Three parallel stratigraphic sections (HC1, HC2, and HC3) were measured from
229 the Horseshoe Creek locality; as these sections were only a few hundred meters apart
230 they are shown as a composite section in Fig. 2. The lower ~73.5 m consists of variably
231 exposed, monotonous grey-green siltstone and shale with occasional thin (<10 cm)
232 lenticular or planar beds of very fine- to fine-grained quartz-rich lithic arenites. These
233 sandstone intervals are locally erosive and host parallel-lamination or occasional very
234 fine ripple cross-lamination with abundant shale partings. Some of the more massive
235 siltstone intervals are locally interspersed with starved ripples of very-fine grained
236 sandstone, but many of the sedimentary structures in the siltstones are masked by a
237 pervasive penetrative cleavage.

238 Numerous discontinuous limestone-bearing beds, 3–70 cm thick, occur
239 sporadically within the massive siltstone and shale units. Many of these carbonate beds
240 are broadly nodular or irregular in geometry and locally grade into pure siltstone, both
241 vertically and laterally. Some carbonate-rich horizons essentially mimic starved ripples
242 and other sedimentary structures characteristic of surrounding siliciclastic beds (Fig. 3A),
243 consistent with post-depositional diagenetic carbonate precipitation. A diagenetic origin
244 for these discontinuous layers is also supported by petrographic observations and
245 microscale SEM-EDS mapping (Figs. 3C, 4). For example, evidence for diagenetic

246 carbonate emplacement includes both the restriction of these Kungarra carbonates to
247 lenses and thin layers intermixed with detrital grains (Figs. 3C, 4) and the distribution
248 within these lenses of patchy carbonate in overgrowth and cement-filling textures within
249 a matrix of silt-sized quartz grains, clay minerals, and rare other silicates (Figs. 3C, 4).
250 Figure 4 shows a representative carbonate layer (green) that includes many detrital
251 silicate grains (orange). A diagenetic origin for many Kungarra carbonates is consistent
252 with major element abundances reported by Lindsay and Brasier (2002); on average, Ca
253 and Mg together make up less than 15% by weight of sampled lithologies, requiring that
254 carbonates are a subordinate component of the samples.

255 A few limestone beds from the Kungarra Formation are more continuous,
256 relatively pure, and either irregularly laminated or clearly stromatolitic. In particular, a
257 distinct stromatolite unit occurs from ~33.9–34.4 m in section HC3, which progresses
258 from ~10 cm of brown-yellow-colored irregular crinkly lamination with interstitial
259 micrite fill into ~25 cm of discrete ~70 cm wide elongate stromatolites. These structures
260 are draped by peach-colored dolomicrite and transition into two distinct layers of
261 brownish-white ~15–30 cm thick domal stromatolites (Fig. 3B) separated by a horizon of
262 1–4 cm wide and ~10 cm tall, high-inheritance digitate stromatolites. The upper 2–5 cm
263 of the stromatolitic interval is irregular, with local rip-up clasts. Laterally, this
264 stromatolitic interval becomes poorly developed; at section HC2, only the irregular
265 carbonate laminae and small domal stromatolites occur (Fig. 3B), and at section HC1 this
266 unit becomes indistinguishable from other thin carbonate units. The only other location in
267 this section with similar stromatolitic features occurs at ~176 m; however, this microbial
268 unit is poorly developed and much thinner (~10 cm). Unlike the carbonate overgrowths in

269 the siltstone units, these carbonate units were likely primary (although they have since
270 been recrystallized). Thus the carbonate-rich units at Horseshoe Creek reflect both
271 original carbonate sediments as well as later carbonate overgrowths of siliciclastics.

272 The upper ~172 m of the Horseshoe Creek section broadly coarsens upwards into
273 a siliciclastic succession dominated by very fine- to fine-grained sandstone. These strata
274 generally transition from green-grey siltstone and argillite with abundant starved ripples,
275 parallel lamination, ripple cross-lamination, and minor carbonate horizons into a
276 succession dominated by very thin- to thin-bedded quartz-rich lithic arenite and
277 sublitharenite with abundant shale partings. One can distinguish clear smaller-scale 1–5
278 m thick coarsening upwards packages of siltstone and shale into very-fine to fine-grained
279 sandstone, which are superimposed on the broader coarsening upwards sequence on the
280 formation scale.

281

282 *4.2. Kazput Formation, NW Hardey Syncline*

283 *4.2.1. Kazput Section #1 (K1)*

284 The K1 section (Figs. 5A, 6) was measured on the NE-dipping flank of a NNW-
285 SSE-striking anticline in the southeastern part of the Hardey Syncline (locality 3 on Fig.
286 1). The base of this section is covered by alluvium, so its relationship to the underlying
287 Koolbye Formation is unclear. The section begins with a prominent bench of dark grey
288 parallel-laminated limestone, about 1.5 m thick (Fig. 5B), that is overlain by ~6 m of
289 sandy limestone with evidence for soft-sediment deformation. The carbonate strata
290 become increasingly sand-rich and dolomitic upsection until, by ~16.5 m, they are
291 dominated by medium-bedded brown dolomitic sandstone. The outcrop then disappears

292 into cover for ~30 meters, but thin-bedded, often calcareous, sandstone horizons are
293 occasionally visible in subcrop (Fig. 5A). Continuous outcrop reappears at 52.5 m, again
294 consisting of interbedded finely laminated calcareous sandstone and brown
295 dolograine. The overlying 30 m consists of brown-weathering (white on fresh
296 surface), coarsely recrystallized dolomite with no visible sedimentary structures. At 86.8
297 m the recrystallization fabric disappears and dolostone displays crinkly lamination and
298 roll-up structures that resemble microbially influenced sedimentary structures. In
299 addition, interbedded chert-replaced rip-ups and intraformational conglomerates occur
300 with other indicators of traction load deposition, including ripple and trough cross-
301 stratified dolograine, channelized grainstone, and thin channelized sandstone lenses
302 (Fig. 5C). Starting at 116.7 m, the section becomes dominated by wavy laminated
303 dolomite, with abundant pisoids and oncoids (up to a cm in diameter), and domal
304 stromatolites up to 30–50 cm wide. A small fault cuts the section at ~127.5 m rendering
305 thickness measurements of the uppermost part of the succession less reliable. At a
306 minimum, an additional 10 m of small conical stromatolites, oncoids, and massive grey
307 dolomite cap the section. Pervasive recrystallization of Kazput Formation carbonates
308 dominates petrographic fabrics, but the interlocking calcite euhedra still preserve mm-
309 scale features such as bedding lamination, coated grains, and ooids.

310

311 *4.2.2 Kazput Section #2 (K2)*

312 The K2 composite section (Figs. 7A, 8, 9) was measured on the SW-dipping flank
313 of the anticline in the central part of the Hardey Syncline (Locality 2 on Fig. 1). The K2
314 section includes two ridges (Fig. 7A) separated by a small valley filled by alluvial

315 material (likely the surficial expression of a fault), so the stratigraphy is represented
316 herein as a composite section (K2A, K2A2, and K2B–K2C; Figs. 8, 9).

317 The basal portion of section K2A (Fig. 8) consists of highly fractured and
318 oxidized maroon and olive green siltstone and shale subcrop exposed in a small, south-
319 flowing dry creek bed at the core of the anticline. Fine-grained deposits transition
320 upsection into ~18 m of olive green to dark grey, parallel laminated to ripple cross-
321 laminated micritic limestone with locally-abundant silt and very fine-grained quartz sand.
322 The basal carbonate-rich strata are thinly bedded and record discrete mm- to cm-scale
323 alternations between massive and laminated beds that resemble the discrete Bouma C-E
324 subdivisions of distal turbidites. The central ~6 m of these more carbonate-rich strata are
325 dominated by pure olive green siltstone with minor detrital carbonate, and the upper 5–6
326 m of these strata record the local development of hummocky cross-stratification and
327 occasional stoss-preservational ripple cross-lamination in the silty limestone deposits.
328 The upper ~45 m of section K2A consists of a broad coarsening-upwards package of
329 olive green to dark grey siltstone and argillite and minor thin-bedded light brown very-
330 fine- to fine-grained quartz sandstone (Fig. 7B). The sandstone beds generally display
331 evidence for subtle scouring of underlying siltstone and argillite intervals and the units
332 are dominated by hummocky and swaley cross-stratification. Sedimentary structures in
333 the siltstone and argillite strata are difficult to discern due to a pervasive penetrative
334 cleavage, but they occasionally contain thin (< 5 cm thick) stringers of nodular and planar
335 micritic limestone. The silica- and carbonate-cemented sandstones of the Kazput
336 Formation can generally be classified as quartz-rich sublitharenites (Martin et al., 2000),

337 but they are mostly dominated by moderately sorted and subrounded to angular
338 monocrystalline quartz sand with minor lithics, chert, and a pervasive chloritic matrix.

339 Since the upper part of section K2A was exposed on a prominent dip slope that
340 projected into a small, faulted alluvial valley, a parallel section was measured to the
341 northwest on the other side of the structure, section K2A2 (Fig. 8). A ~6 m thick package
342 of pure olive green siltstone was used to trace the section over the projected small fault
343 horizon. This section begins with ~17 m of dark grey-green siltstone and argillite that
344 progressively becomes increasingly carbonate rich. Thin (2–3 cm thick) stringers of
345 nodular to stratiform, silty micritic limestone thicken upsection into parallel-laminated
346 and ripple cross-laminated beds up to 10 cm thick. These silty limestone deposits are
347 abruptly overlain by ~4 m of peach-orange to blue-grey-colored fine-grained
348 dolograine with abundant ripple cross-lamination and minor detrital silt and quartz
349 sand. Locally, there are thin (<20 cm) horizons with irregular and wavy lamination that
350 resemble microbial carbonates. The upper portion of this small section becomes heavily
351 dolomitized, although there are multiple horizons with crenulated or wavy laminae and
352 intervals of detrital silt and quartz sand that form discrete lenses and stringers within the
353 carbonate laminae. A massive, light bluish-grey colored dolostone horizon was used to
354 trace this section over to section K2B.

355 Section K2B forms the base of a large hill and K2B/C comprises over 65 m of
356 interbedded carbonate and siliciclastic deposits with some evidence for syndimentary
357 slumping and faulting (Figs. 7A, D, 9). The lowermost 21 m of K2B strata are composed
358 of silty to fine-grained sandy limestone with mm-scale parallel lamination, ripple cross-
359 lamination, and low-angle bedding truncations (Fig. 7B) interbedded with two carbonate-

360 dominated units: a) fine-grained micritic limestones with wavy laminae, crenulated
361 laminae, and small slumps from syn-sedimentary faults; and b) finely-laminated silty to
362 sandy carbonates with low angle hummocky and swaley cross stratification (Fig. 7C).
363 The wavy laminated carbonates often form thin (up to a few cm) stromatolites, which can
364 follow relict topography (Fig. 10B) or become contorted, folded, or faulted (syn-
365 sedimentary). These cm-scale stromatolite layers become thicker and well developed
366 higher in the section. Above the interbedded silty and stromatolitic carbonates is a thick
367 (~15 m) interval of well-sorted, fine- to medium-grained sandstone, in decimeter-scale
368 beds with ripple and hummocky cross-stratification.

369 A similar succession of silty and stromatolitic carbonates capped by thick
370 sandstone occurs again in the K2C section; however, the internal structure of the silty
371 carbonate is more massive than those lower in the section. Higher in the section (around
372 45 m), the stromatolitic units develop into thick, well-defined, meter-scale stromatolite
373 domes (Fig. 10). These large stromatolites are commonly contorted and occasionally cut
374 by neptunian dykes (e.g. Fig. 10E). Interbedded with and above the large stromatolitic
375 domes are wave-rippled and hummocky cross-stratified silty sandstones. Beds are often
376 amalgamated, making bedding thickness difficult to discern. A further silty sandstone at
377 the top of the section is distinguished by carbonate intraclasts one centimeter to several
378 meters in length and typically rounded or tabular in shape (Fig. 9). The clasts consist of
379 stromatolites and other carbonate lithologies observed lower in the section, as well as
380 recrystallized oolitic grainstones that broadly link the two measured Kazput sections.

381

382 **5. Results: Carbon isotope chemostratigraphy**

383 *5.1. Kungarra carbonates*

384 Lindsay and Brasier (2002) reported carbon isotopic abundances for 22 carbonate
385 samples distributed through an estimated 250 m of stratigraphy at Horseshoe Creek,
386 reported as Kazput Formation but now known to belong to the Kungarra Formation.
387 Their $\delta^{13}\text{C}$ values ranged from -6 to +2‰, varying in sawtooth fashion through the
388 reported section. Our larger sample set ($n = 125$) is consistent with measurements by
389 Lindsay and Brasier (2002); $\delta^{13}\text{C}$ values for Kungarra carbonates at Horseshoe Creek
390 exhibit a wide range of isotopic values, from -6.3‰ to +0.5‰, with no strong
391 stratigraphic trend (Fig. 2). The $\delta^{18}\text{O}$ values for the same samples range from -6.15‰ to -
392 1.61‰, again with no strong trend (see supplemental data). In contrast to Lindsay and
393 Brasier (2002), our denser sampling coverage across multiple spatial scales enables us to
394 detect variations in the carbon isotope results of up to 2‰ between lighter (more
395 carbonate) and darker (less carbonate) layers within a single hand sample, as much as 4‰
396 between samples from closely spaced sections at a single stratigraphic horizon, and
397 equally strong variation between samples spaced stratigraphically only centimeters to a
398 few meters apart (Fig. 2, supplemental data).

399

400 *5.2. Kazput carbonates*

401 All $\delta^{13}\text{C}$ values measured for Kazput carbonates in the Hardey Syncline ($n = 252$)
402 fall between -4.5‰ and +2‰, and all but a stratigraphically constrained subset lie
403 between -0.5‰ and +1.5‰ (Figs. 6, 8, 9). These results are consistent with
404 reconnaissance analyses by Bekker et al. (2002). $\delta^{18}\text{O}$ values range from -8.13‰ to -
405 16.63‰, with most values falling between -15.5‰ and -16.5‰ (see supplemental data).

406 At the base of section K1 (Fig. 6), $\delta^{13}\text{C}_{\text{carb}}$ values are low (around -4‰); whereas
407 the last data point before the prominent covered interval is more moderate at 0.7‰.
408 Above the covered interval, $\delta^{13}\text{C}_{\text{carb}}$ values are again depleted (-3‰) but quickly return to
409 values between 0 and 1‰ for the remainder of the section (Fig. 6). The $\delta^{13}\text{C}_{\text{carb}}$ signature
410 of section K2 begins much like that of K1, with negative values (-2.5‰ to -1.2‰) in the
411 lowermost 10 m (K2A, Fig. 8) followed by values that fluctuate around 0‰ (K2A and
412 K2A2, Fig. 8). Higher in the section (K2B and K2C), C-isotopic values generally
413 fluctuate between ca. 0.5 and 1.5‰, with a few more negative values interspersed
414 through the sections (Fig. 9). Variations of up to 1‰ among carbonate intraclasts at the
415 top of the section likely reflect the heterogeneous stratigraphic levels from which the
416 intraclasts and carbonate blocks were sourced.

417 Petrographic subsampling of stromatolites at 46–47 m of K2C shows limited
418 isotopic variation among microfacies, with stromatolitic carbonates slightly heavier than
419 the carbonate-rich clastics that overlie the stromatolites (Fig. 9). As might be predicted
420 when ambient waters are strongly oversaturated with respect to calcite and aragonite
421 (Bergmann et al., 2013), carbonates within stromatolites differ little from encompassing
422 laminae in both their carbon and oxygen isotope values (Fig. 9). The analyzed Kazput
423 carbonates do not record the extreme ^{13}C enrichment that defines the younger
424 Lomagundi-Jatuli event.

425

426 **6. Results: Kazput stromatolites**

427 The most notable sedimentary features of the Kazput carbonates are m-scale
428 domal stromatolites in section K2B/C (Fig. 10). These stromatolites appear to have

429 nucleated on erosional surfaces within underlying siliciclastic units and were, in turn,
430 episodically buried by further influx of sands that locally display hummocky cross-
431 stratification. The resulting microbialites can be as thin as a centimeter (Fig 10B),
432 suggesting only a limited time for accretion between inundation events, to as much as 1.5
433 meters thick (Fig 10A).

434 Two fabrics make up the Kazput stromatolites (see Section 7.3 for genetic
435 interpretations): wavy to crenulated siliciclastic laminae, 30 to 400 μm thick, that are
436 continuous on the scale of a single dome, and interbedded, convex upward, lenticular
437 carbonates that are generally discontinuous on a mm to cm-scale and are common or
438 absent in alternating zones (Fig. 10). The discrete fabrics are clear in both optical
439 microscopic view (Fig. 11) and in elemental maps using SEM (Fig. 12). Lamina-rich
440 zones tend to be <1 cm to about 2 cm thick, whereas zones rich in lenticular carbonate
441 vary from <1 cm to, more commonly, 10–15 cm thick. Because silicate laminae are more
442 resistant to erosion than carbonate lenses, the broad mesoscale fabric of the stromatolites
443 is best observed on weathered surfaces; lamina-rich zones are darker brown and more
444 resistant, carbonate-rich zones are grey or lighter tan and more recessive (Fig. 10). For
445 the most part, lenticular carbonates occur within 5–15 mm long convex-upward mini-
446 domes bounded by laterally linked laminae that tend to be continuous across the surfaces
447 on which they occur. In some layers, lenses extend laterally for several cm along bedding
448 planes (Fig 10D); however, these occurrences are rare. Most of the stromatolitic
449 structures are irregular, and some show evidence of plastic deformation (folds and
450 slumps). At a few horizons, however, more or less regular, laterally linked columns

451 develop either locally (Fig. 10F) or across a stromatolitic dome surface (Fig 10D);
452 columns are 5–8 cm wide and 2–10 cm high.

453 At the microscopic scale, laminae contain an admixture of several minerals,
454 including equant calcite anheda, 10–25 μm in maximum dimension; quartz silt; clay
455 minerals (commonly chloritized, but also including Mg-rich species); and small opaque
456 euhedra, probably originally diagenetic pyrite, but now altered to iron oxides (Figs. 11,
457 12). While clays can form authigenically within microbialites (Konhauser and Urrutia,
458 1999; L veill  et al., 2000) the presence of abundant fine-grained quartz grains and other
459 detrital material indicates the incorporation of suspension load siliciclastics, even when
460 traction load sands were absent. Organic carbon inclusions also occur sporadically
461 throughout the K2 stromatolites; these appear as black spots on the composite elemental
462 map or red spots on the carbon map in Figure 12.

463 Lenticular units generally consist of interlocking calcite anheda 25–100 μm in
464 maximum dimension. Pyrite, reduced carbon, and clay minerals also occur in these zones,
465 although at low abundances (Fig. 12). The coarsely crystalline carbonates reflect
466 pervasive diagenetic and/or metamorphic recrystallization, but mm-scale banding is
467 preserved locally (Fig 11C). Crystals are smaller in these banded carbonates, generally
468 less than 25 μm , and discrete zones are defined by both larger and smaller crystals
469 (lighter and darker zones in Fig 11C), as well as a faint tendency for smaller crystals to be
470 oriented along laminae surfaces.

471 The stromatolites form irregular, m-scale domes on flat-lying surfaces or arches
472 over relict seafloor relief; local reorientation and folding indicate slumping during or
473 shortly after accretion. Like the smaller scale fabrics, at the decimeter to meter scale these

474 stromatolitic domes are variable in shape, but heritability is much higher. The domes are
475 capped by and often interbedded with hummocky cross-stratified sandstones. Clastic-
476 filled neptunian dykes occur sporadically through the section (Fig. 10E). The dykes
477 typically cut at a high angle through the undeformed stromatolite layers, but can run
478 parallel to lamination in cement-poor intervals. In aggregate, these features are plausibly
479 explained by a composite structure that combined rigid penecontemporaneous cements
480 with more plastic silt- and clay-rich laminae, as discussed below.

481

482 **7. Discussion**

483 *7.1 Kungarra carbonates*

484 Broadly, Kungarra Formation strata record a major coarsening upwards sequence
485 from banded iron formation and starved basin deposits of the underlying Boolgeeda Iron
486 Formation through glaciomarine deposits of the Meteorite Bore Member and finally into
487 tidal flat, beach, and fluvial deposits of the overlying Koolbye Formation (Mazumder et
488 al., 2015). The measured Horseshoe Creek section (Fig. 2) captures a small component of
489 this broad coarsening upwards trend. The abundance of fine-grained suspension deposits
490 interbedded with starved ripple and planar ripple cross-laminated sandstone intervals
491 most likely represents subtidal deposition between storm and fair weather wave base.
492 This is consistent with the limited development of stromatolites. The lack of directly
493 overlying shoreface deposits suggests that deposition was predominantly in an offshore
494 setting, although the increase in sandstone intervals and the broad coarsening upwards
495 trend in the upper ~25 m of the measured section is diagnostic of progradation. Given
496 these features, we suggest these strata were largely deposited in a prodeltaic or mid-outer

497 shelf environment, broadly consistent with the interpretations of previous workers
498 (Krapež, 1996; Martin et al., 2000; Van Kranendonk et al., 2015).

499 As noted above, Lindsay and Brasier (2002) sampled the carbonate-bearing rocks
500 at Horseshoe Creek, and the highly variable carbon isotope values were interpreted to
501 indicate pronounced carbon cycle variation in the aftermath of the GOE. However,
502 regional mapping has shown that the strata in question lie stratigraphically beneath the
503 Meteorite Bore Member and so are properly assigned to the Kungarra Formation
504 (Krapež, 1996; Martin et al., 2000; Van Kranendonk et al., 2015). Furthermore,
505 stratigraphic field relationships and detailed petrology both suggest that most of these
506 Kungarra carbonates formed during diagenesis, and the marked C-isotopic variation
507 recorded in these rocks confirms this interpretation (Figs 2–4). $\delta^{13}\text{C}$ values of -6‰ are
508 unusual for carbonates of any age and commonly reflect the incorporation of isotopically
509 light carbon into diagenetic carbonates precipitated within sediments (Irwin et al., 1977).
510 Within Lindsay and Brasier's (2002) plotted stratigraphic column, $\delta^{13}\text{C}$ values commonly
511 vary by several per mil from one sample to the next. Our more detailed data set enables
512 us to document large carbon isotopic variations (up to 4‰) within hand samples and
513 between samples from the same stratigraphic horizon (Fig. 2). Such fine-scale spatial and
514 temporal variation is essentially impossible to accommodate in terms of primary C-
515 isotopic signatures reflecting global seawater chemistry.

516 Arguably, the isotopic variation observed at individual horizons in the lower
517 Kungarra Formation of the Horseshoe Creek section reflects diagenetic carbonate
518 precipitation from pore fluids in which dissolved inorganic carbon (DIC) sourced from
519 seawater was variably mixed with inorganic carbon generated by the remineralization of

520 isotopically light organic matter. In this case, the most positive isotope results represent
521 values closest to the dissolved inorganic carbon (DIC) in seawater. Alternatively, if these
522 units underwent episodic subaerial exposure in the Paleoproterozoic, meteoric waters
523 may have altered the isotopic composition of the strata during early diagenesis.
524 Regardless, the isotopic values from the measured Kungarra Formation from the
525 Horseshoe Creek section by and large do not represent the original isotopic composition
526 of seawater during the time of deposition.

527

528 *7.2. Kazput carbonates*

529 Similar to the underlying Kungarra Formation, the ~750 m thick Kazput
530 Formation records a complex depositional history heavily influenced by local
531 synsedimentary tectonism (Krapež, 1996; Martin et al., 2000; Thorne and Tyler, 1996;
532 Thorne et al., 1995). Numerous cm to dm scale synsedimentary normal faults in K2B and
533 K2C indicate the occurrence of active extensional tectonism during Kazput
534 sedimentation. Furthermore, the large stromatolitic clasts and rip-ups (including m-scale
535 rafts that are clearly transported) in the uppermost K2 facies likely represent seismically-
536 generated breccias (seismites) or the erosion of locally uplifted strata. Given the limited
537 stratigraphic range of this study within the Turee Creek Group, it is difficult to provide
538 more context to the greater basinal or tectonic setting of these strata.

539 Given previous descriptions of the basal Kazput succession as a starved basin
540 marked by distinct carbonate rhythmites (e.g., Krapež, 1996), the Kazput sections
541 described here appear to lie relatively close to the base of the formation. The parallel-
542 laminated and turbiditic silty limestone units that mark the base of the two measured

543 sections suggest a relatively quiet-water environment. At both localities, the rocks
544 quickly transition upsection into fine-grained siliciclastic units with abundant evidence
545 for storm-generated bedforms, indicative of higher energy/shallower water conditions.
546 The remainder of the measured sections can be interpreted as a broad shallowing upward
547 succession of mixed carbonate and siliciclastic strata. The abundance of fine-grained
548 shale and siltstone interbedded with hummocky and swaley cross-stratification in the
549 central part of the sections suggests subtidal deposition on a storm-dominated shelf
550 between storm and fair weather wave base. The establishment of this subtidal shelf
551 setting was relatively short-lived because both Kazput sections record relatively abrupt
552 shoaling into shallow-water shoreface and platformal settings. This is clearly evidenced
553 by the deposition of thick peritidal to subtidal platformal carbonate dominated by ooids,
554 oncoids, and coarse dolograins in section K1 (Fig. 6) and a more complex mixed
555 sandstone-stromatolitic limestone sequence in section K2 (Figs. 8, 9).

556 The striking difference in siliciclastic composition between the upper portions of
557 the two parallel sections (K1 and K2) is problematic; however, given the complexity and
558 heterogeneity of along-strike facies and possible proximity to a shoreline, it is reasonable
559 to conclude that their differences are primarily due to proximity to siliciclastic point
560 sources, such as nearby deltaic systems. In fact, section K2 preserves many of the
561 hallmarks of high sedimentation rates in a tectonically active basin, such as thick
562 sequences of stoss-preservational ripple cross-lamination and abundant syndimentary
563 dykes and soft-sediment deformation. The intimate association of unique stromatolite
564 morphologies and abundant trough cross-stratified sandstone intervals in the upper K2
565 interval also suggests deposition in a shoreface setting subject to periodically high

566 sedimentation rates. We note that carbonate lithologies differ between sections K1 and
567 K2, with stromatolite development limited to the latter. We cannot rule out the possibility
568 that the two sections are not strictly coeval, but prefer to interpret these facies as
569 contemporaneous expressions of carbonate deposition in a spatially heterogeneous and
570 rapidly developing basin.

571 Unlike the results from the Kungarra Formation carbonates, the Kazput isotope
572 data are interpreted to indicate dominantly primary seawater values. The agreement of
573 values from closely spaced samples and the consistent trends suggest that diagenetic
574 overprinting of the isotopic signal was minimal. Furthermore, no petrographic results
575 suggest secondary calcite overgrowths, which are clearly documented in the Kungarra
576 carbonates (Fig. 3). Thus, the C-isotopic values of -1 to -3‰ in lowermost Kazput
577 carbonates could record transiently low $\delta^{13}\text{C}$ in contemporaneous seawater. Above this
578 horizon, however, values hover between 0.5‰ and 1.5‰ through the remainder of the
579 succession.

580

581 *7.3. Kazput stromatolites*

582 The striking m-scale stromatolite domes of the Kazput Formation (Fig. 10) exhibit
583 features that are typically associated with microbial carbonates, but are unique in
584 containing such an abundance of lensoidal calcite precipitates. Laminae in these
585 structures are interpreted as the sedimentary manifestation of mat-building microbial
586 communities. Beyond their general similarity to laminae observed in stromatolites
587 throughout the Proterozoic Eon, a mat origin is supported by at least four observations:
588 (1) the irregular and commonly distorted surfaces of laminae indicate formation by

589 materials that were both coherent and flexible; (2) quartz silt and, very likely, clay
590 minerals within laminae indicate the trapping and binding of introduced materials; (3)
591 laminae contain a higher concentration of reduced carbon than associated microfibrils,
592 consistent with an origin as mats; and (4) laminae contain localized high concentration of
593 (originally) pyrite, suggesting decay within mats via microbial sulfate reduction. The
594 microbial mats likely nucleated on sandy substrates, forming wrinkled mats (wrinkle
595 structures or laminae) and cm-scale stromatolites (Fig 10B); larger structures resulted
596 from protracted growth between episodes of sand deposition. Based on petrographic and
597 elemental analysis, the quartz silt and clay minerals that are found within the
598 stromatolites indicate that suspension load siliciclastics were continuously deposited on
599 mat surfaces during stromatolite growth.

600 An outstanding question is the extent to which the lenticular carbonates found
601 between laminae formed on, or just beneath, mat surfaces or filled primary voids formed
602 by gas emission within mats. Gas-generated voids occur sporadically throughout the
603 Proterozoic stromatolite record. Their formation generally requires strong but flexible
604 mats populated by filamentous microorganisms, gas generation (e.g., oxygenic
605 photosynthesis, decomposition of organic matter, or methanogenesis), and seawater that
606 is strongly oversaturated with respect to calcium carbonate minerals (e.g., Knoll et al.,
607 2013; Mata et al., 2012). Indeed, primary voids in Archean stromatolites have been
608 interpreted as *prima facie* evidence for oxygenic photosynthesis at 3 Ga (Bosak et al.,
609 2009, 2010). The carbonate precipitates do not crosscut microbial laminae, eliminating
610 dissolution and subsequent in-filling as an explanation for the observed textures.

611 Given that the Kazput stromatolites lie within rocks deposited stratigraphically
612 after the GOE, all aforementioned requirements for the formation and preservation of
613 primary voids appear to have been met locally. The irregular, convex upward
614 morphology of laminae is consistent with this interpretation, as is the orientation of zoned
615 cements in some stromatolites (Fig. 11C, E). However, the lateral extent of discrete
616 cement horizons that occasionally contain clay, pyrite, and reduced carbon flecks also
617 supports the alternative interpretation that the cements are seafloor precipitates formed on
618 or within surface mats (e.g., Fig. 11B). In fact, the two interpretations are not mutually
619 exclusive; if the waters that bathed the Kazput bioherms were strongly supersaturated
620 with respect to calcium carbonate, both void-forming and cementing processes may have
621 been operating during stromatolite accretion.

622 Stromatolites are found widely in late Archean and Paleoproterozoic carbonates,
623 with particularly good descriptions of macro- and microstructure available for late
624 Archean microbialites from the Gamohaam and Frisco formations of the
625 Campbellrand/Malmani succession, South Africa (Sumner, 1997), and lower
626 Paleoproterozoic carbonates from the Fennoscandian Shield (McLoughlin et al., 2013).
627 What differentiates the Kazput stromatolites from most of these (and essentially all
628 younger Proterozoic) structures is their abundance of lenticular carbonate. Microdigitate
629 stromatolites, some of them small microbial structures and others stacked crystal fans
630 (Grotzinger and Knoll, 1999), are particularly widespread in Paleoproterozoic carbonate
631 successions (Medvedev et al., 2005). These structures formed widely across shallow
632 shelves and platforms and reflect a high degree of oversaturation with respect to calcium
633 carbonate minerals. Thus, they are relevant to the interpretation of the Kazput structures,

634 but differ in lacking the regular interlamination of microbial laminae and precipitates
635 described here.

636 Perhaps the closest approximation of the composite laminar-lenticular Kazput
637 fabric is found in cusped microbialites from the Campbellrand/Malmani succession
638 (Sumner, 1997) and elsewhere in late Archean carbonates (e.g., Hofmann and Masson,
639 1994; Riding et al., 2014). In these structures, void spaces that originated by the draping
640 of pliant mats across vertical microbial “tent poles” were filled penecontemporaneously
641 by carbonate cement (Sumner, 1997). Locally, stromatolites in the 2720 ± 5 Ma
642 Tumbiana Formation, Fortescue Group, Western Australia, also contain thin, irregular
643 patches of carbonate precipitates, interpreted as lake-floor precipitates (Flannery and
644 Walter, 2012; Lepot et al., 2008, 2009). The Kazput and Tumbiana stromatolites do share
645 some similarities, such as the weathering profile (prominent laminae and recessive
646 cements) and the μm -scale banded carbonate domes within carbonate-rich layers;
647 however, there are important distinctions between the two. Kazput stromatolites do not
648 contain halite pseudomorphs, nor is there evidence for the penecontemporaneous erosion
649 of carbonate precipitates, as is clearly evident in the Tumbiana stromatolites (Lepot et al.,
650 2008, 2009). Furthermore, the Kazput stromatolites cements are largely discrete (mm- to
651 cm-scale) lenses and typically do not form thick, continuous cement laminae as in the
652 Tumbiana examples. These examples underscore the importance of macroscopic
653 carbonate precipitates in generating fabrics within late Archean/early Paleoproterozoic
654 stromatolites; nonetheless, the specific alternation of particle-binding mats and lenticular
655 carbonate precipitates is, to the best of our knowledge, a unique feature of Kazput

656 stromatolites in the Hardey Syncline, reflecting a potentially time-limited interaction
657 between the evolving biota and its physical surroundings.

658

659 *7.4. Chemostratigraphic comparisons*

660 Few carbon isotopic data are available for carbonates that unambiguously lie
661 above Paleoproterozoic iron formations but below glaciogenic rocks. Samples from the
662 poorly dated Boxelder Creek Formation, South Dakota (Bekker et al., 2003a) and
663 Polisarka Sedimentary Formation in drill cores from the Kola Peninsula, Russia (Brasier
664 et al., 2013), span a range of -6‰ to 1‰. Carbonates of the Gandarela Formation, Brazil,
665 are isotopically similar, but cannot be placed unambiguously relative to Paleoproterozoic
666 ice ages. Post-glacial marbles of the Paleoproterozoic Sauser Group, India, also show C-
667 isotopic values of -3.1‰ to +2.6‰ above a moderately negative basal interval (-4.4‰ to
668 -7.4‰) interpreted as a cap carbonate (Mohanty et al., 2015). The most positive C-
669 isotopic values for Kungarra carbonates are consistent with the values reported from
670 other basins, but the uncertainties introduced by diagenetic carbonate precipitation limit
671 what the Kungarra samples can add to discussions about the post-BIF, pre-GOE carbon
672 cycle.

673 On the basis of limited data, Karhu and Holland (1996) hypothesized that the
674 strongly positive carbon isotopic excursion called the Lomagundi-Jatuli event began ca.
675 2.2 Ga. Even now, isotopic data are sparse for successions younger than GOE
676 onset/glaciogenic rocks but older than 2200 Ma. Martin et al. (2013) summarized
677 available radiometric constraints on the Lomagundi-Jatuli event, concluding that the
678 event began between 2306 ± 9 Ma and 2221 ± 5 Ma and ended between 2106 ± 8 and

679 2057 ± 1 Ma, for a maximum duration of 249 ± 9 million years and a minimum duration
680 of 128 ± 9.4 million years. The new data presented herein are consistent with these age
681 constraints, and provide no evidence for strongly positive Lomagundi-Jatuli δ¹³C values
682 during deposition of the measured Kazput sections. We recognize, however, that our
683 sections represent a limited proportion of the time interval between Paleoproterozoic ice
684 ages and events commencing at 2200 Ma; regionally, Kazput carbonates are separated
685 from the Cheela Springs basalt and its intrusive counterpart (2209 ± 15 Ma; Martin et al.,
686 1998) by thick siliciclastic deposits and a major unconformity (Fig. 1). Thus, while these
687 new data demonstrate that the interval between the GOE onset/glacials and 2200 Ma
688 includes a time where the seawater DIC isotopic composition was unperturbed and
689 similar to modern isotopic values, we cannot rule out the possibility that it also includes
690 short intervals of positive C-isotopic excursions, which are not recorded in the analyzed
691 Kazput Formation sections.

692 Kazput carbonates are isotopically similar to those of well-developed carbonates
693 in the Gandarela Formation, Brazil, where 163 samples show values near 0‰ (Bekker et
694 al., 2003b; Maheshwari et al., 2010). The Gandarela carbonates (Babinski et al., 1995) lie
695 stratigraphically above major BIF and below carbonates that show Lomagundi-type ¹³C
696 enrichment, but the regional stratigraphy contains no glacial diamictites; Bekker et al.
697 (2003b) cite a Pb-Pb date of 2420 ± 19 Ma for Gandarela carbonates, but this does not
698 appear in Martin et al.'s (2013) review due to the low confidence in the interpretation of
699 Pb-Pb carbonate dates in Proterozoic successions. The well-studied Deutschland
700 Formation, dated indirectly at 2316 ± 7 Ma by Re-Os on black shale of the possibly
701 correlative Rooihoogte-Timeball Hill Formation (Hannah et al., 2004), bears ¹³C

702 enrichments up to 10.1‰ in its upper part (Bekker et al., 2001). However, the Mooidraai
703 Dolomite (diagenetic age of 2394 ± 26 Ma, based on carbonate-bound Pb), also in South
704 Africa, appears to have no isotopic anomalies, with $\delta^{13}\text{C}$ values of 0.5 to 1‰, more
705 similar to those of the Kazput Formation (Bau et al., 1999). Clearly, tighter radiometric
706 constraints will be necessary to validate interbasinal correlations and accurately
707 reconstruct early Paleoproterozoic carbon cycle dynamics.

708

709 **8. Conclusions**

710 This study provides new litho- and chemostratigraphic data for carbonate-bearing
711 intervals of the 2.45–2.22 Ga Turee Creek Group, Western Australia, which spans a
712 pivotal time in Earth history after the deposition of global banded iron formation and
713 across the GOE. Field relationships, petrography, elemental mapping, and C-isotope
714 values reveal that most Kungarra carbonates in the pre-glacial lower part of the Turee
715 Creek Group formed during syndepositional or post-depositional diagenesis; therefore,
716 the abundant and highly negative C-isotopic values within these rocks cannot be
717 interpreted in terms of global carbon cycle dynamics, as previously assumed by Lindsay
718 and Brasier (2002).

719 In contrast, carbonates from the lower part of the uppermost Kazput Formation of
720 the Turee Creek Group — which sits in a globally under-sampled interval above
721 Paleoproterozoic glacial deposits and below an unconformity constrained by the ~2.2 Ga
722 Cheela Springs Basalt and associated sills — do appear to record the C isotopic
723 composition of seawater DIC, with consistent $\delta^{13}\text{C}$ values of -2 to +1.5‰. As the lower
724 parts of the Kazput Formation likely represent a relatively brief time interval, it

725 strengthens a growing body of evidence indicating that the initial geochemical signature
726 of the GOE and the exceptionally positive values of the Lomagundi-Jatuli isotope
727 excursion(s) are separated by one or more intervals of normal C isotopic composition.

728 The moderate C-isotopic values of Turee Creek Group carbonates strengthen the
729 argument that the complex set of processes that drove the onset of the GOE did not
730 include anomalously high proportional rates of organic carbon burial. Of course, as others
731 have noted (e.g., Lyons et al., 2014; and references therein), it is not required that the
732 increase in Paleoproterozoic oxygen concentrations was limited to the brief interval
733 marked by the end of mass-independent S isotope fractionation, nor that oxygen change
734 was monotonic (Canfield, 2014; Canfield et al., 2013; Lyons et al., 2014). Instead, the
735 MIF-S signature might reflect an interval of atmospheric oxygen accumulation that was
736 neither large nor rapid but crossed an important threshold. One would expect pO_2 to
737 continue to rise during the Lomagundi-Jatuli event (e.g., Bekker and Holland, 2012;
738 Kump et al., 2011; Rasmussen et al., 2013), but any increase in oxygen levels driven by
739 extensive organic carbon burial postdates the MIF-S boundary, very likely by tens of
740 millions of years (see also Martin et al., 2013).

741 Beyond the perspective on Paleoproterozoic carbon cycle dynamics provided by
742 the stable carbon isotopic data, Turee Creek Group carbonates host unusual, if not
743 unique, stromatolites that are geobiologically informative. Notably, Kazput stromatolites
744 contain a high volume of precipitated carbonate—indeed, more abundant than the
745 siliciclastic-rich laminae in many horizons (Fig. 10). As noted above, this reflects locally
746 abundant seafloor precipitates and/or penecontemporaneous filling of primary voids
747 formed by microbial gas release. The most comparable structures are precipitate-rich

748 cusplate Archean microbialites from South Africa (Sumner, 1997) and late Archean
749 Tumbiana stromatolites from Western Australia (Flannery and Walter, 2012; Lepot et al.,
750 2008, 2009). Whatever their proper mechanistic interpretation, the Kazput Formation
751 stromatolites in the Hardey Syncline are morphologically distinct, reflecting a potentially
752 time-limited interaction between the evolving biota and its physical surroundings.

753

754 **Acknowledgements**

755 We thank R. Shapiro and an anonymous reviewer for constructive comments on
756 an earlier version of this paper. We thank the Agouron Institute for funding the 2012
757 Advanced Geobiology Course to Australia, Henry Goodall and Guy L'Estrange for
758 logistical support, and Sarah Manley for running the carbon isotope analyses. R.
759 Martindale thanks Dr. A. H. Knoll and the NASA Astrobiological Institute for providing
760 postdoctoral funding. J. Strauss and K. French acknowledge NSF graduate research
761 fellowships for funding support. E. Sperling thanks the Agouron Institute for an Agouron
762 Postdoctoral Fellowship. D. Flannery was supported by the University of New South
763 Wales and the Australian Centre for Astrobiology. M. Walter acknowledges a
764 Professorial Fellowship from the Australian Research Council. R. Mazumder is grateful
765 to the University of New South Wales and Agouron Institute for support. M. Van
766 Kranendonk also acknowledges funding support from the University of New South
767 Wales.

768 **References**

- 769 Akin, S.J., Pufahl, P.K., Hiatt, E.E., Pirajno, F., 2013. Oxygenation of shallow marine
770 environments and chemical sedimentation in Paleoproterozoic peritidal settings: Frere
771 Formation, Western Australia. *Sedimentology* 60, 1559-1582.
- 772 Asael, D., Tissot, F.L.H., Reinhard, C.T., Rouxel, O., Dauphas, N., Lyons, T.W.,
773 Ponzevera, E., Liorzou, C., Chéron, S., 2013. Coupled molybdenum, iron and uranium
774 stable isotopes as oceanic paleoredox proxies during the Paleoproterozoic Shunga Event.
775 *Chemical Geology* 362, 193-210.
- 776 Babinski, M., Chemale Jr, F., Van Schmus, W.R., 1995. The Pb/Pb age of the Minas
777 Supergroup carbonate rocks, Quadrilátero Ferrífero, Brazil. *Precambrian Research* 72,
778 235-245.
- 779 Barley, M.E., Pickard, A.L., Sylvester, P.J., 1997. Emplacement of a large igneous
780 province as a possible cause of banded iron formation 2.45 billion years ago. *Nature* 385,
781 55–58.
- 782 Bau, M., Romer, R.L., Lüders, V., Beukes, N.J., 1999. Pb, O, and C isotopes in silicified
783 Moidraai dolomite (Transvaal Supergroup, South Africa): implications for the
784 composition of Paleoproterozoic seawater and ‘dating’ the increase of oxygen in the
785 Precambrian atmosphere. *Earth and Planetary Science Letters* 174, 43-57.
- 786 Bekker, A., Holland, H.D., 2012. Oxygen overshoot and recovery during the early
787 Paleoproterozoic. *Earth and Planetary Science Letters* 317–318, 295-304.
- 788 Bekker, A., Holland, H.D., Wang, P.-L., Rumble, D., Stein, H.J., Hannah, J.L., Coetzee,
789 L.L., Beukes, N.J., 2004. Dating the rise of atmospheric oxygen. *Nature* 427, 117-120.

790 Bekker, A., Karhu, J.A., Eriksson, K.A., Kaufman, A.J., 2003a. Chemostratigraphy of
791 Paleoproterozoic carbonate successions of the Wyoming Craton: tectonic forcing of
792 biogeochemical change? *Precambrian Research* 120, 279-325.

793 Bekker, A., Kasting, J., Anbar, A., 2013. Evolution of the atmosphere and ocean through
794 time. *Chemical Geology* 362, 1-2.

795 Bekker, A., Kaufman, A.J., Karhu, J.A., Beukes, N.J., Swart, Q.D., Coetzee, L.L.,
796 Eriksson, K.A., 2001. Chemostratigraphy of the Paleoproterozoic Duitschland Formation,
797 South Africa: Implications for coupled climate change and carbon cycling. *American*
798 *Journal of Science* 301, 261-285.

799 Bekker, A., Krapež, B., Karhu, J.A., 2002. Preliminary chemostratigraphic data on
800 carbonates from the Paleoproterozoic Turee Creek Supersequence and Woolly Dolomite
801 of Western Australia. 16th International Sedimentologic Congress Abstract Volume, 26-
802 27.

803 Bekker, A., Sial, A.N., Karhu, J.A., Ferreira, V.P., Noce, C.M., Kaufman, A.J., Romano,
804 A.W., Pimentel, M.M., 2003b. Chemostratigraphy of carbonates from the Minas
805 Supergroup, Quadrilátero Ferrífero, Brazil: A stratigraphic record of early Proterozoic
806 atmospheric, biogeochemical and climatic change. *American Journal of Science* 303,
807 865-904.

808 Bergmann, K.D., Grotzinger, J.P., Fischer, W.W., 2013. Biological influences on seafloor
809 carbonate precipitation. *Palaios* 28, 99-115.

810 Blake, T.S., Barley, M.E., 1992. Tectonic evolution of the late Archaean to early
811 Proterozoic Mount Bruce mega sequence set, Western Australia. *Tectonics* 11, 1415-
812 1425.

813 Bosak, T., Bush, J., Flynn, M., Liang, B., Ono, S., Petroff, A.P., Sim, M.S., 2010.
814 Formation and stability of oxygen-rich bubbles that shape photosynthetic mats.
815 *Geobiology* 8, 45–55.

816 Bosak, T., Liang, B., Sim, M.S., Petroff, A.P., 2009. Morphological record of oxygenic
817 photosynthesis in conical stromatolites. *Proceedings of the National Academy of*
818 *Sciences* 106, 10939–10943.

819 Brasier, A.T., Martin, A.P., Melezhik, V.A., Prave, A.R., Condon, D.J., Fallick, A.E.,
820 2013. Earth's earliest global glaciation? Carbonate geochemistry and geochronology of
821 the Polisarka Sedimentary Formation, Kola Peninsula, Russia. *Precambrian Research*
822 235, 278-294.

823 Canfield, D.E., 2014. *Oxygen: A Four Billion Year History*. Princeton University Press,
824 Princeton, New Jersey.

825 Canfield, D.E., Ngombi-Pemba, L., Hammarlund, E.U., Bengtson, S., Chaussidon, M.,
826 Gauthier-Lafaye, F., Meunier, A., Riboulleau, A., Rollion-Bard, C., Rouxel, O., Asael,
827 D., Pierson-Wickmann, A.-C., El Albani, A., 2013. Oxygen dynamics in the aftermath of
828 the Great Oxidation of Earth's atmosphere. *Proceedings of the National Academy of*
829 *Sciences* 110, 16736-16741.

830 Farquhar, J., Bao, H., Thiemens, M., 2000. Atmospheric influence of Earth's earliest
831 sulfur cycle. *Science* 289, 756–758.

832 Flannery, D.T., Walter, M.R., 2012. Archean tufted microbial mats and the Great
833 Oxidation Event: new insights into an ancient problem. *Australian Journal of Earth*
834 *Sciences* 59, 1-11.

835 Fralick, P.W., Poulton, S.W., Canfield, D.E., 2011. Does the Paleoproterozoic Animikie
836 Basin record the sulfidic ocean transition?: COMMENT. *Geology* 39, e241.

837 Grotzinger, J.P., Knoll, A.H., 1999. Stromatolites in Precambrian carbonates:
838 Evolutionary mileposts or environmental dipsticks? *Annual Review of Earth and*
839 *Planetary Sciences* 27, 313-358.

840 Halverson, G.P., Shields-Zhou, G., 2011. Chapter 4 Chemostratigraphy and the
841 Neoproterozoic glaciations. Geological Society, London, *Memoirs* 36, 51-66.

842 Hannah, J.L., Bekker, A., Stein, H.J., Markey, R.J., Holland, H.D., 2004. Primitive Os
843 and 2316 Ma age for marine shale: implications for Paleoproterozoic glacial events and
844 the rise of atmospheric oxygen. *Earth and Planetary Science Letters* 225, 43-52.

845 Hoffman, P.F., 2013. The Great Oxidation and a Siderian snowball Earth: MIF-S based
846 correlation of Paleoproterozoic glacial epochs. *Chemical Geology* 362, 143-156.

847 Hofmann, H.J., Masson, M., 1994. Archean stromatolites from the Abitibi greenstone
848 belt, Quebec, Canada. *Geological Society of America Bulletin* 106, 424-429.

849 Horwitz, R.C., 1982. Geological history of the Early Proterozoic Paraburdoo Hinge Zone,
850 Western Australia. *Precambrian Research* 19, 191-200.

851 Hotinski, R.M., Kump, L.R., Arthur, M.A., 2004. The effectiveness of the
852 Paleoproterozoic biological pump: A $\delta^{13}\text{C}$ gradient from platform carbonates of the
853 Pethei Group (Great Slave Lake Supergroup, NWT). *Geological Society of America*
854 *Bulletin* 116, 539-554.

855 Irwin, H., Curtis, C., Coleman, M., 1977. Isotopic evidence for source of diagenetic
856 carbonates formed during burial of organic-rich sediments. *Nature* 269, 209-213.

857 Johnston, D.T., Macdonald, F.A., Gill, B.C., Hoffman, P.F., Schrag, D.P., 2012.
858 Uncovering the Neoproterozoic carbon cycle. *Nature* 483, 320-323.

859 Karhu, J.A., Holland, H.D., 1996. Carbon isotopes and the rise of atmospheric oxygen.
860 *Geology* 24, 867-870.

861 Kaufman, A.J., Hayes, J.M., Klein, C., 1990. Primary and diagenetic controls of isotopic
862 compositions of iron-formation carbonates. *Geochimica et Cosmochimica Acta* 54,
863 3461–3473.

864 Kirschvink, J.L., Gaidos, E.J., Bertani, L.E., Beukes, N.J., Gutzmer, J., Maepa, L.N.,
865 Steinberger, R.E., 2000. Paleoproterozoic snowball Earth: Extreme climatic and
866 geochemical global change and its biological consequences. *Proceedings of the National*
867 *Academy of Sciences, U.S.A.* 97, 1400–1405.

868 Knoll, A.H., Beukes, N.J., 2009. Introduction: Initial investigations of a Neoproterozoic shelf
869 margin-basin transition (Transvaal Supergroup, South Africa). *Precambrian Research*
870 169, 1-14.

871 Knoll, A.H., Wörndle, S., Kah, L.C., 2013. Covariance of microfossil assemblages and
872 microbialite textures across an upper Mesoproterozoic carbonate platform. *Palaios* 28,
873 453-470.

874 Konhauser, K.O., Lalonde, S.V., Planavsky, N.J., Pecoits, E., Lyons, T.W., Mojzsis, S.J.,
875 Rouxel, O.J., Barley, M.E., Rosiere, C., Fralick, P.W., Kump, L.R., Bekker, A., 2011.
876 Aerobic bacterial pyrite oxidation and acid rock drainage during the Great Oxidation
877 Event. *Nature* 478, 369-373.

878 Konhauser, K.O., Urrutia, M.M., 1999. Bacterial clay authigenesis: a common
879 biogeochemical process. *Chemical Geology* 161, 399-413.

880 Krapež, B., 1996. Sequence stratigraphic concepts applied to the identification of basin-
881 filling rhythms in Precambrian successions. *Australian Journal of Earth Sciences* 43,
882 355–380.

883 Kump, L.R., Junium, C., Arthur, M.A., Brasier, A., Fallick, A., Melezhik, V., Lepland,
884 A., Črne, A.E., Luo, G., 2011. Isotopic evidence for massive oxidation of organic matter
885 following the Great Oxidation Event. *Science* 334, 1694-1696.

886 Lepot, K., Benzerara, K., Brown, G.E., Phillipot, P., 2008. Microbially influenced
887 formation of 2,724-million-year-old stromatolites. *Nature Geoscience* 1, 118 - 121.

888 Lepot, K., Benzerara, K., Rividi, N., Cotte, M., Brown Jr, G.E., Philippot, P., 2009.
889 Organic matter heterogeneities in 2.72 Ga stromatolites: Alteration versus preservation
890 by sulfur incorporation. *Geochimica et Cosmochimica Acta* 73, 6579-6599.

891 Lévillé, R.J., Fyfe, W.S., Longstaffe, F.J., 2000. Geomicrobiology of carbonate–silicate
892 microbialites from Hawaiian basaltic sea caves. *Chemical Geology* 169, 339-355.

893 Lindsay, J.F., Brasier, M.D., 2002. Did global tectonics drive early biosphere evolution?
894 Carbon isotope record from 2.6 to 1.9 Ga carbonates of Western Australian basins.
895 *Precambrian Research* 114, 1-34.

896 Lyons, T.W., Reinhard, C.T., Love, G., Xiao, S., 2012. Geobiology of the Proterozoic
897 Eon, in: Knoll, A.H., Canfield, D.E., and Konhauser, K.O. (Ed.), *Fundamentals of*
898 *Geobiology*. Blackwell, pp. 371-402.

899 Lyons, T.W., Reinhard, C.T., Planavsky, N.J., 2014. The rise of oxygen in Earth's early
900 ocean and atmosphere. *Nature* 506, 307-315.

901 Maheshwari, A., Sial, A.N., Gaucher, C., Bossi, J., Bekker, A., Ferreira, V.P., Romano,
902 A.W., 2010. Global nature of the Paleoproterozoic Lomagundi carbon isotope excursion:

903 A review of occurrences in Brazil, India, and Uruguay. *Precambrian Research* 182, 274-
904 299.

905 Martin, A.P., Condon, D.J., Prave, A.R., Lepland, A., 2013. A review of temporal
906 constraints for the Palaeoproterozoic large, positive carbonate carbon isotope excursion
907 (the Lomagundi–Jatuli Event). *Earth-Science Reviews* 127, 242-261.

908 Martin, D.M., 1999. Depositional setting and implications of Paleoproterozoic
909 glaciomarine sedimentation in the Hamersley Province, Western Australia. *Geological*
910 *Society of America Bulletin* 111, 189-203.

911 Martin, D.M., Li, Z.X., Nemchin, A.A., Powell, C.M., 1998. A pre-2.2 Ga age for giant
912 hematite ores of the Hamersley Province Australia? . *Economic Geology* 93, 1084–1090.

913 Martin, D.M., Powell, C.M., George, A.D., 2000. Stratigraphic architecture and evolution
914 of the early Paleoproterozoic McGrath Trough, Western Australia. *Precambrian Research*
915 99, 33-64.

916 Mata, S.A., Harwood, C.L., Corsetti, F.A., Stork, N.J., Eilers, K., Berelson, W.M., Spear,
917 J., 2012. Influences of gas production and filament orientation on stromatolite
918 microfabric. *Palaios* 27, 206-219.

919 Mazumder, R., Van Kranendonk, M.J., Altermann, W., 2015. A marine to fluvial
920 transition in the Paleoproterozoic Koolbye Formation, Turee Creek Group, Western
921 Australia. *Precambrian Research* 258, 161–170.

922 McLoughlin, N.J., Melezhik, V.A., Brasier, A.T., Medvedev, P.V., 2013.
923 Palaeoproterozoic stromatolites from the Lomagundi-Jatuli interval of the Fennoscandian
924 Shield., in: A. Prave, A.E.F., V.A. Melezhik, A. Lepland, E.J. Hanski, & H. Strauss (Ed.),
925 *Reading the archive of Earth's oxygenation: Global events and the Fennoscandian Arctic*

926 Russia - Drilling Early Earth Project (FAR-DEEP) (Frontiers in Earth Sciences, 3).
927 Springer, Heidelberg, pp. 1298-1351.

928 Medvedev, P., Bekker, A., Karhu, J.A., Kortelainen, N., 2005. Testing the
929 biostratigraphic potential of early Paleoproterozoic microdigitate stromatolites. *Revista*
930 *Española de Micropaleontología* 37, 41-56.

931 Melezhik, V.A., Fallick, A.E., 2010. On the Lomagundi-Jatuli carbon isotopic event: The
932 evidence from the Kalix Greenstone Belt, Sweden. *Precambrian Research* 179, 165-190.

933 Mohanty, S.P., Barik, A., Sarangi, S., Sarkar, A., 2015. Carbon and oxygen isotope
934 systematics of a Paleoproterozoic cap-carbonate sequence from the Sausar Group,
935 Central India. *Palaeogeography, Palaeoclimatology, Palaeoecology* 417, 195-209.

936 Müller, S.G., Krapež, B., Barley, M.E., Fletcher, I.R., 2005. Giant iron-ore deposits of
937 the Hamersley province related to the breakup of Paleoproterozoic Australia: New
938 insights from in situ SHRIMP dating of baddeleyite from mafic intrusions. *Geology* 33,
939 577-580.

940 Partin, C.A., Lalonde, S.V., Planavsky, N.J., Bekker, A., Rouxel, O.J., Lyons, T.W.,
941 Konhauser, K.O., 2013. Uranium in iron formations and the rise of atmospheric oxygen.
942 *Chemical Geology* 362, 82-90.

943 Planavsky, N.J., Asael, D., Hofmann, A., Reinhard, C.T., Lalonde, S.V., Knudsen, A.,
944 Wang, X., Ossa, F.O., Pecoits, E., Smith, A.J.B., Beukes, N.J., Bekker, A., Johnson,
945 T.M., Konhauser, K.O., Lyons, T.W., Rouxel, O.J., 2014. Evidence for oxygenic
946 photosynthesis half a billion years before the Great Oxidation Event. *Nature Geoscience*
947 7, 283-286.

948 Planavsky, N.J., Bekker, A., Hofmann, A., Owens, J.D., Lyons, T.W., 2012. Sulfur
949 record of rising and falling marine oxygen and sulfate levels during the Lomagundi event.
950 Proceedings of the National Academy of Sciences 109, 18300-18305.

951 Powell, C.M., Horwitz, R.C., 1994. Late Archaean and early Proterozoic tectonics and
952 basin formation of the Hamersley Ranges, Twelfth Australian Geological Convention,
953 Perth, Geological Society of Australia (WA Division), Excursion Guidebook, 4, p. 53.

954 Pufahl, P.K., Hiatt, E.E., 2012. Oxygenation of the Earth's ocean-atmosphere system: a
955 review of physical and chemical sedimentological responses. Marine and Petroleum
956 Geology 32, 1-20.

957 Pufahl, P.K., Hiatt, E.E., Kyser, T.K., 2010. Does the Paleoproterozoic Animikie Basin
958 record the sulfidic ocean transition? Geology 38, 659-662.

959 Pufahl, P.K., Hiatt, E.E., Kyser, T.K., 2011. Does the Paleoproterozoic Animikie Basin
960 record the sulfidic ocean transition? REPLY. Geology 39, e242-e243.

961 Rasmussen, B., Bekker, A., Fletcher, I.R., 2013. Correlation of Paleoproterozoic
962 glaciations based on U–Pb zircon ages for tuff beds in the Transvaal and Huronian
963 Supergroups. Earth and Planetary Science Letters 382, 173-180.

964 Reinhard, C.T., Planavsky, N.J., Robbins, L.J., Partin, C.A., Gill, B.C., Lalonde, S.V.,
965 Bekker, A., Konhauser, K.O., Lyons, T.W., 2013. Proterozoic ocean redox and
966 biogeochemical stasis. Proceedings of the National Academy of Sciences 110, 5357-
967 5362.

968 Riding, R., Fralick, P., Liang, L., 2014. Identification of an Archean marine oxygen oasis.
969 Precambrian Research 251, 232-237.

970 Scott, C., Wing, B.A., Bekker, A., Planavsky, N.J., Medvedev, P., Bates, S.M., Yun, M.,
971 Lyons, T.W., 2014. Pyrite multiple-sulfur isotope evidence for rapid expansion and
972 contraction of the early Paleoproterozoic seawater sulfate reservoir. *Earth and Planetary*
973 *Science Letters* 389, 95-104.

974 Sumner, D.Y., 1997. Late Archean calcite-microbe interactions: Two morphologically
975 distinct microbial communities that affected calcite nucleation differently. *Palaios* 12,
976 302-318.

977 Swanner, E.D., Planavsky, N.J., Lalonde, S.V., Robbins, L.J., Bekker, A., Rouxel, O.J.,
978 Saito, M.A., Kappler, A., Mojzsis, S.J., Konhauser, K.O., 2014. Cobalt and marine redox
979 evolution. *Earth and Planetary Science Letters* 390, 253-263.

980 Takehara, M., Komure, M., Kiyokawa, S., Horie, K., Yokohama, K., 2010. Detrital
981 zircon SHRIMP U–Pb age of the 2.3Ga diamictites of the Meteorite Bore Member in the
982 South Pilbara, Western Australia., in: Tyler, I.M., Knox-Robinson, C.M. (Eds.), *Fifth*
983 *International Archean Symposium Abstracts: Geological Survey of Western Australia,*
984 *Record 2010/18*, pp. 223–222.

985 Thorne, A.M., 1990. Ashburton Basin, in *Geology and Mineral Resources of Western*
986 *Australia: Geological Survey of Western Australia, Memoir 3*, 210-219.

987 Thorne, A.M., Seymour, D.B., 1991. *Geology of the Ashburton Basin Western Australia:*
988 *Geological Survey of Western Australia, Bulletin 139.*

989 Thorne, A.M., Tyler, I.M., 1996. Roy Hill, Western Australia Sheet 50-12: *Geological*
990 *Survey of Western Australia, 1:250 000 map series.*

991 Thorne, A.M., Tyler, I.M., Blight, D.F., 1995. Rocklea, Western Australia: *Geological*
992 *Survey of Western Australia, 1:100 000 geological series.*

993 Trendall, A.F., 1969. Three great basins of Precambrian banded iron formation
994 deposition: A systematic comparison. *Geological Society of America Bulletin* 79, 1527-
995 1544.

996 Trendall, A.F., 1976. Striated and faceted boulders from the Turee Creek Formation –
997 Evidence for a possible Huronian glaciation on the Australian continent, *Geological*
998 *Survey of Western Australia Annual Report* 1975, pp. 88-92.

999 Trendall, A.F., 1979. A revision of the Mount Bruce Supergroup. *Geological Survey of*
1000 *Western Australia Annual Report* 1978, 63–71.

1001 Trendall, A.F., 1981. The Lower Proterozoic Meteorite Bore Member, Hamersley Basin,
1002 Western Australia, in: Hambrey, M.J., Harland, W.B. (Eds.), *Earth's Pre-Pleistocene*
1003 *glacial record*. Cambridge University Press, Cambridge, pp. 555–557.

1004 Trendall, A.F., 1990. Hamersley Basin, in *Geology and Mineral Resources of Western*
1005 *Australia*. Geological Survey of Western Australia, Memoir 3, 163-190.

1006 Trendall, A.F., Blockley, J.G., 1970. The iron formations of the Precambrian Hamersley
1007 Group, Western Australia with special reference to the crocidolite. *Geological Survey of*
1008 *Western Australia, Bulletin* 119, 1-366.

1009 Trendall, A.F., Trendall, A.F., Morris, R.C., 1983. Chapter 3 The Hamersley Basin,
1010 *Developments in Precambrian Geology*. Elsevier, pp. 69-129.

1011 Tyler, I.M., Thorne, A.M., 1990. The northern margin of the Capricorn Orogen, Western
1012 Australia—an example of an Early Proterozoic collision zone. *Journal of Structural*
1013 *Geology* 12, 685-701.

1014 Van Kranendonk, M., 2010. Three and a half billion years of life on Earth: A transect
1015 back in time. *Geological Survey of Western Australia Record* 2010/21.

1016 Van Kranendonk, M.J., Altermann, W., Beard, B.L., Hoffman, P.F., Johnson, C.J.,
1017 Kasting, J.F., Melezhik, V.A., Nutman, A.P., Papineau, D., Pirajno, F., 2012. A
1018 chronostratigraphic division of the Precambrian: possibilities and challenges, in:
1019 Gradstein, F.M., Ogg, J.G., Schmitz, M.D., Ogg, G.J. (Eds.), *The Geologic Time Scale*
1020 2012. Elsevier, Boston, USA, pp. 299–392.

1021 Van Kranendonk, M.J., Mazumder, R., 2015. Two Paleoproterozoic glacio-eustatic
1022 cycles in the Turee Creek Group, Western Australia. *Geological Society of America*
1023 *Bulletin* 127, 596-607.

1024 Van Kranendonk, M.J., Mazumder, R., Yamaguchi, K.E., Yamada, K., Ikehara, M.,
1025 2015. Sedimentology of the Paleoproterozoic Kungarra Formation, Turee Creek Group,
1026 Western Australia: A conformable record of the transition from early to modern Earth.
1027 *Precambrian Research* 256, 314-343.

1028 Williford, K.H., Van Kranendonk, M.J., Ushikubo, T., Kozdon, R., Valley, J.W., 2011.
1029 Constraining atmospheric oxygen and seawater sulfate concentrations during
1030 Paleoproterozoic glaciation: In situ sulfur three-isotope microanalysis of pyrite from the
1031 Turee Creek Group, Western Australia. *Geochimica et Cosmochimica Acta* 75, 5686-
1032 5705.

1033

1034

1035 **Figure captions**

1036 Figure 1. Geographic, stratigraphic, and geological location of the studied sections.
1037 Upper left: Location of study area in Australia (star). Upper right: stratigraphic context
1038 for the Turee Creek Group; stars indicate stratigraphic horizons of studied sections.
1039 Bottom: Geological map of the Hardey Syncline from Martin et al. (2000); numbered
1040 circles indicate studied localities.

1041

1042 Figure 2. Litho- and chemostratigraphy of the Kungarra Formation section at Horseshoe
1043 Creek (composite section of stratigraphic columns HC1, HC2, and HC3). The
1044 stratigraphic interval between 33.9 m and 34.4 m has been enlarged to show the
1045 succession of stromatolitic textures (interpreted to be of microbial origin). Inset images
1046 are photomicrographs (plane polarized light) of the Kungarra carbonates; sample HC2
1047 12.5A is from 13.8 m and HC3 40.2 is from 40.2 m. Dots in inset images indicate
1048 microsampling locations and their carbon isotope values.

1049

1050 Figure 3. Kungarra Formation carbonates at Horseshoe Creek. A) Pinkish-white micritic
1051 limestone interbedded with reddish-brown fine-grained sandstone forming starved
1052 ripples, Australian dollar for scale (25 mm diameter). B) Close up of stromatolites from
1053 roughly 34.2 m in stratigraphic height, Australian dollar for scale. C) Petrographic view
1054 of the domal stromatolite layer (Sample HC3 34.3, 34.3m in stratigraphic height),
1055 showing overgrowths of calcite on micritic carbonates stained by iron oxides (note scale
1056 bar).

1057

1058 Figure 4. Elemental map of Kungarra Formation limestone (sample HC3 16.25 from
1059 16.25m in stratigraphic height); top images are the entire sample, and the bottom images
1060 are close up views of the boxed area. On the left are SEM images, on the right are false
1061 color representations of the elemental maps, and the middle images are a composite
1062 image of the SEM images and elemental maps. Note that the calcium (calcite) only
1063 manifests in rare lenses with abundant detrital minerals, suggesting that it is not primary
1064 carbonate but rather diagenetic.

1065

1066 Figure 5. Lithologies of the Kazput Formation in Hardey Syncline section K1. A)
1067 Overview of stratigraphy, section K1 begins in the thin-bedded limestones in the
1068 foreground, the base of the cliff is at 53 m elevation in the stratigraphic column (Fig. 6),
1069 and the measured section continues up the gully on the left. B) Close-up of thin-bedded
1070 limestones at the base of the K1 section, hammer for scale. C) Cross-stratified
1071 grainstones with abundant bed-parallel silicification at meter 108 in the K1 section,
1072 Sharpie tip for scale.

1073

1074 Figure 6. Litho- and chemostratigraphy of the Kazput Formation at section K1.

1075

1076 Figure 7. Lithologies of the Kazput Formation in Hardey Syncline section K2. A)
1077 Overview of stratigraphy, showing where individual subsections were measured. B) Fine
1078 grained, parallel-laminated facies in section K2A, Australian dollar for scale (25 mm
1079 diameter). C) Section K2B; silty to (fine) sandy carbonates with small-scale ripples in the
1080 lower half of the photo and mm-scale laminations in the upper half. Blue ruler at the

1081 bottom of the photo is 10.5 cm long. D) Interbedded sandy carbonates and fine-grained
1082 carbonates with wavy to stromatolitic laminae (section K2B); rock hammer for scale.

1083

1084 Figure 8. Litho- and chemostratigraphy of the Kazput Formation at sections K2A and
1085 K2A2. Note that K2A2 sits stratigraphically above the K2A section.

1086

1087 Figure 9. Litho- and chemostratigraphy of Kazput Formation at sections K2B and K2C.
1088 Expanded section in upper right highlights geochemical results from stromatolite
1089 microsampling.

1090

1091 Figure 10. Kazput stromatolites. A) Large domal stromatolites forming over relict
1092 topography at 47 m stratigraphic height (in section K2C). B) Thin stromatolite layer
1093 within fine-grained micritic limestones; note the eroded base on which the stromatolite
1094 accreted. C) Alternating layers of siliciclastic lamina-rich (resistant) and carbonate-rich
1095 (recessive) layers within the larger stromatolites; note the weathering difference between
1096 units. D) Top layers of domal stromatolites from K2C (47 m), note the alternating layers
1097 of siliciclastic lamina-rich and carbonate-rich layers. The stromatolites on the top layer
1098 formed much larger (>5 cm), more cement-rich structures than earlier layers. E)
1099 Syndimentary neptunian dyke through stromatolite layers, dark patches are shadows
1100 from vegetation on the outcrop. F) Domal stromatolites growing into microdigitate
1101 stromatolites within cement-rich intervals of the large domal stromatolites in K2C.

1102

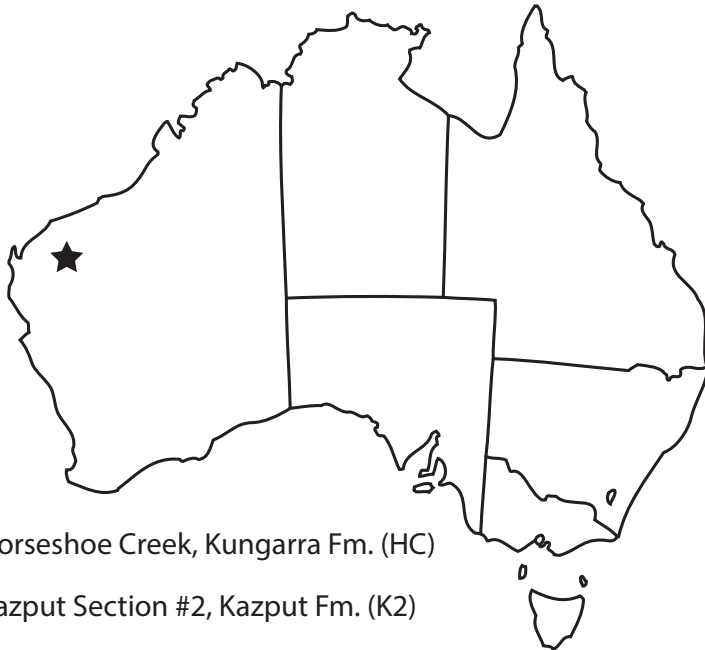
1103 Figure 11. Petrographic textures of Kazput stromatolites (all plane polarized light). A)
1104 Alternating siliciclastic lamina-rich and discontinuous carbonate-rich layers of large
1105 domal stromatolites from section K2C (47 m, sample K2C 5.5B2); B) Unusually
1106 continuous carbonate-rich layers in section K2C (65.7 m, sample K2C 31.8m); C)
1107 Microstructure of a transported and rolled up stromatolite, showing the local preservation
1108 of fine banding in lenticular carbonate precipitates highlighted by arrows (63.4 m, sample
1109 K2C 28.6); D) Detail of a siliciclastic-rich lamina in a small stromatolite containing
1110 quartz, pyrite, and clay minerals, with carbonate-rich areas above and below (Sample
1111 K2C 28.5); E) Close up of Fig. 11C highlighting the faint banding within the carbonate
1112 fabric of the deformed stromatolite (63.4 m sample K2C 28.6).

1113

1114 Figure 12. Elemental map of Kazput Formation stromatolitic carbonates (sample KAZS1,
1115 47 m height in section K2C); top row is an image of the entire sample, and the middle
1116 and bottom rows are close up views of boxes 1 and 2 respectively. Left column are SEM
1117 images, right column images are false color representations of the elemental maps, and
1118 the middle illustrations are composite images of the elemental and SEM maps. Note,
1119 unlike the Kungarra Fm. (Fig. 4), calcium (calcite) is the dominant mineral with quartz
1120 and aluminosilicates occurring with high relative abundance in stromatolitic laminae.
1121 Small iron oxide grains (blue in false color maps) occur throughout the Kazput section
1122 but are concentrated in silicate-rich laminae (orange in false color maps). There are also
1123 organic carbon inclusions throughout the section (see second row); they appear as black
1124 spots in the composite figure and are highlighted in red on the carbon (C) elemental map.

1125

Figure 1



- ① Horseshoe Creek, Kungarra Fm. (HC)
- ② Kazput Section #2, Kazput Fm. (K2)
- ③ Kazput Section #1, Kazput Fm. (K1)

Wyloo Group	Mount McGrath Formation
	Cheela Springs Basalt (2209 ± 15 Ma)
Turee Creek Group	Beasley River Quartzite
	Kazput Formation ★
	Koolbye Formation
	Kungarra Formation Meteorite Bore Mb. ★
Hamersley Group	Boolgeda Iron Formation
	Woongarra Rhyolite (2449 ± 3 Ma)
	Weeli Wolli Formation

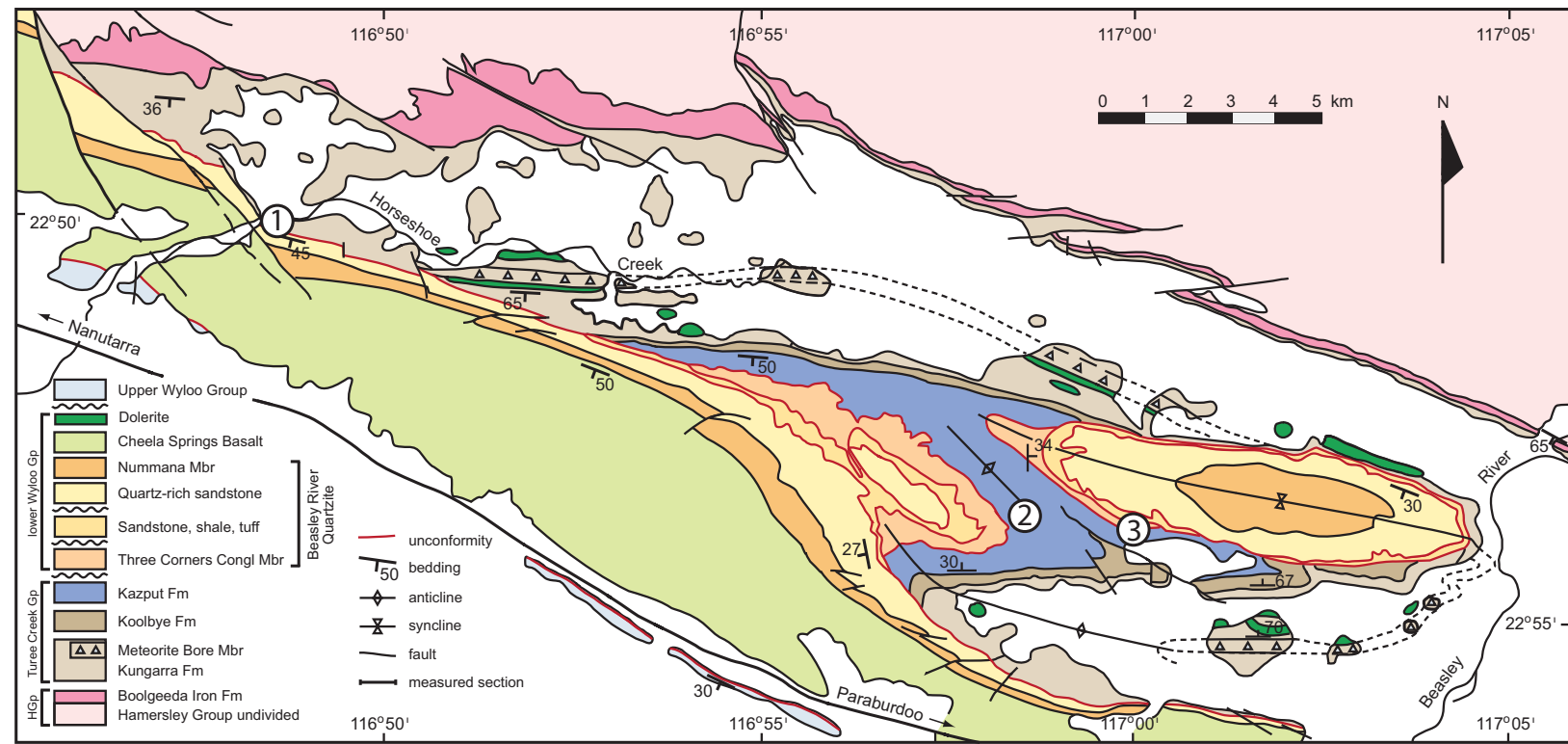


Figure 2

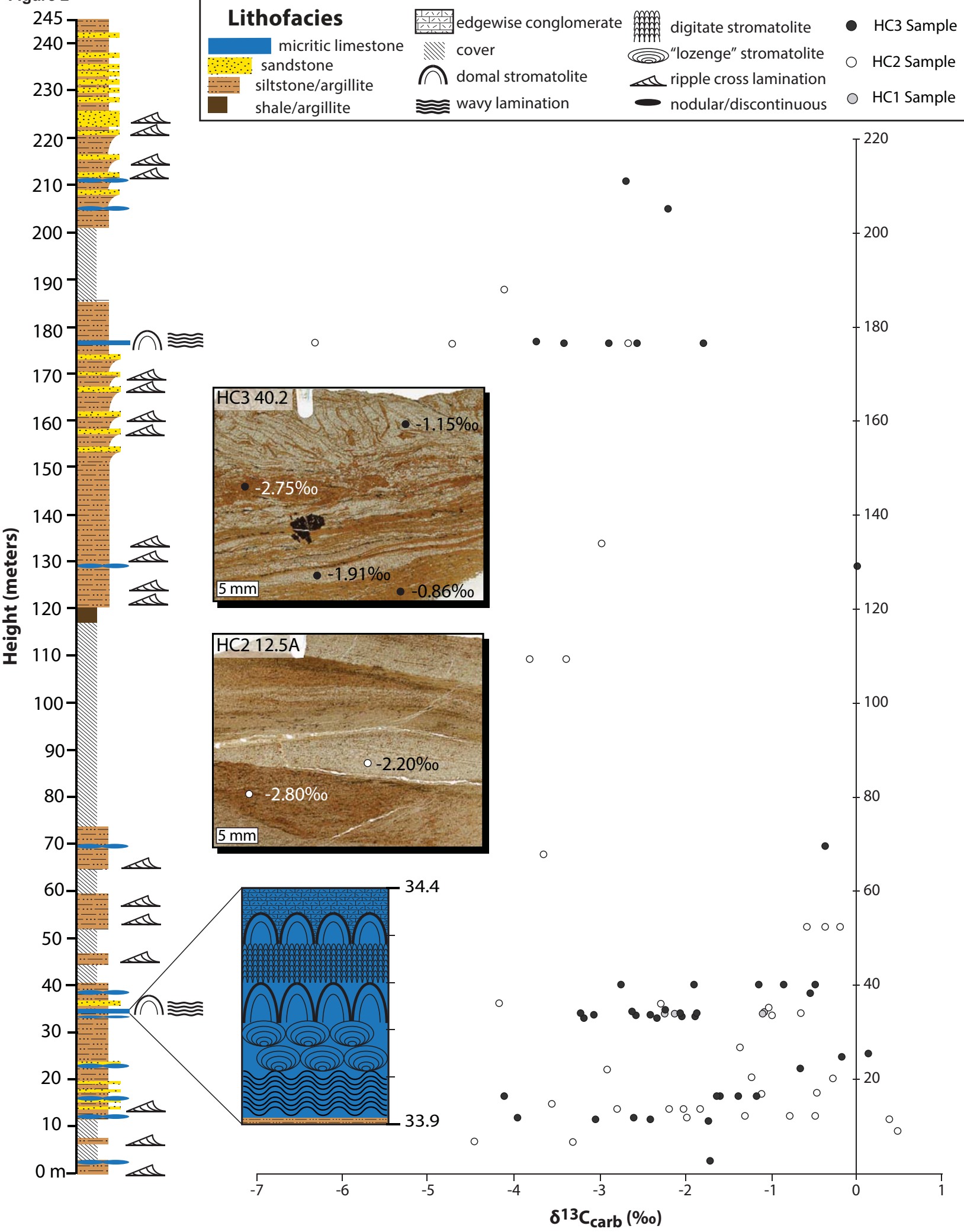


Figure 3
[Click here to download high resolution image](#)

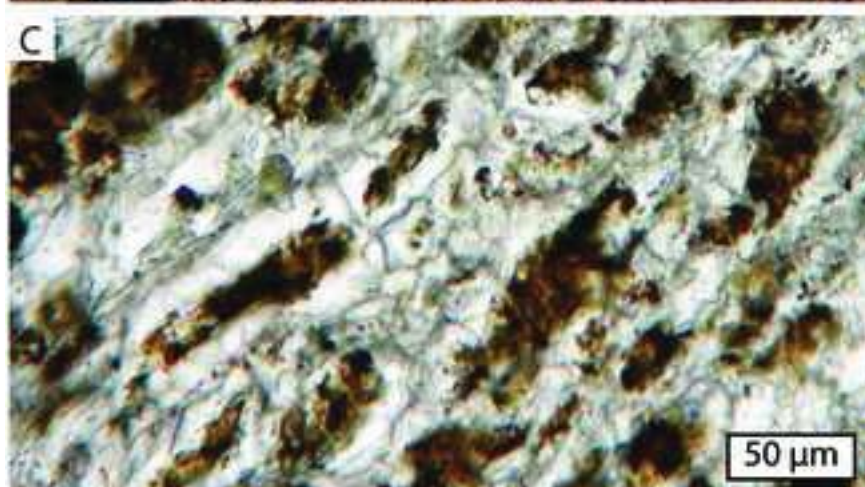


Figure 4

HC3 16.25m - Kungarra carbonate

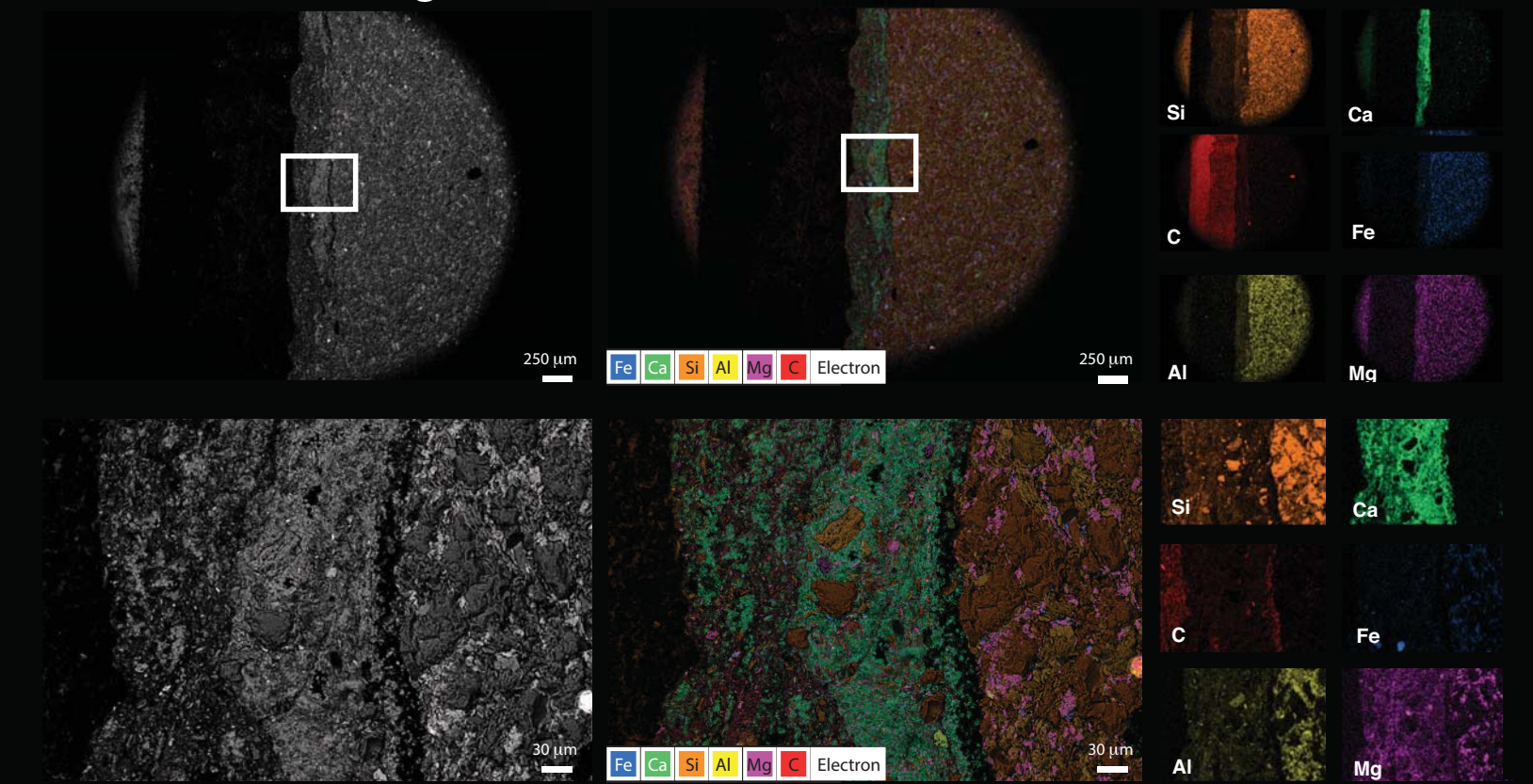
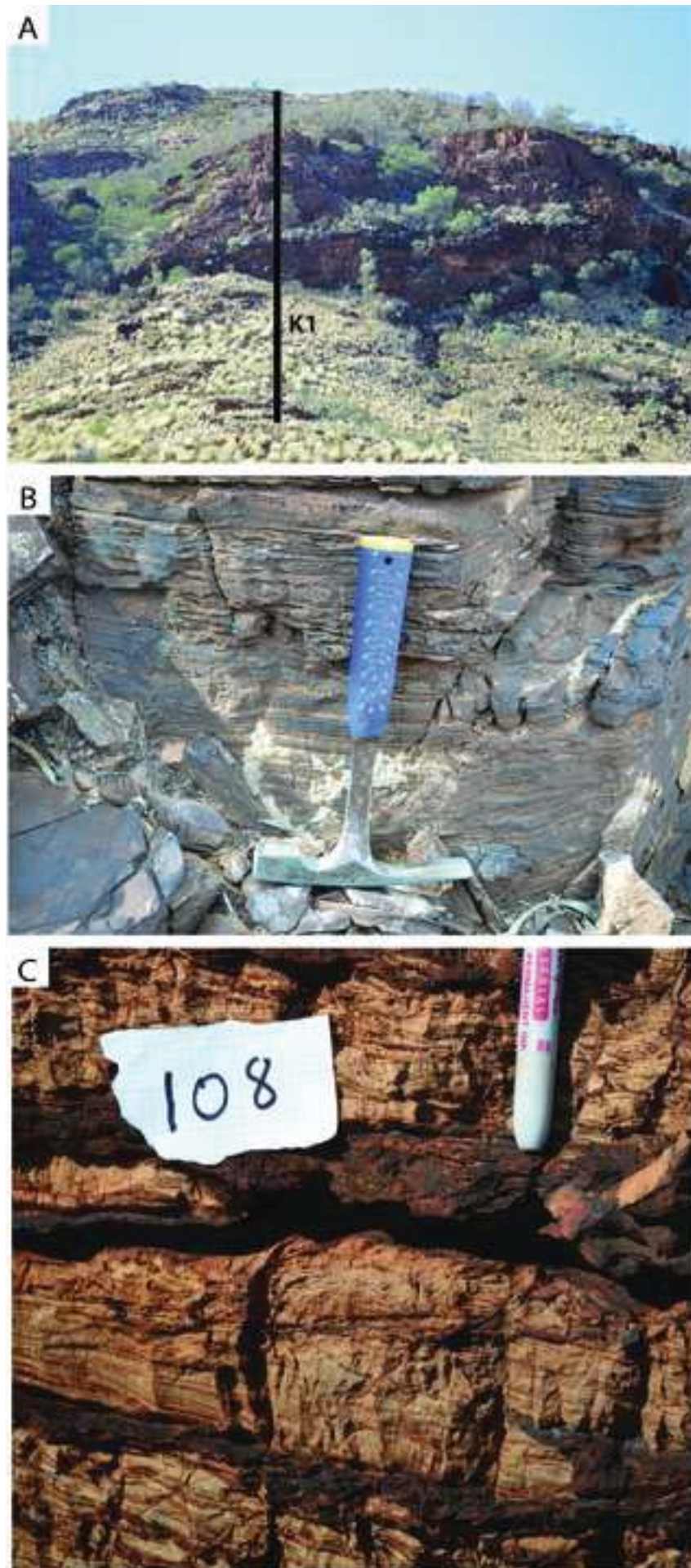


Figure 5
[Click here to download high resolution image](#)



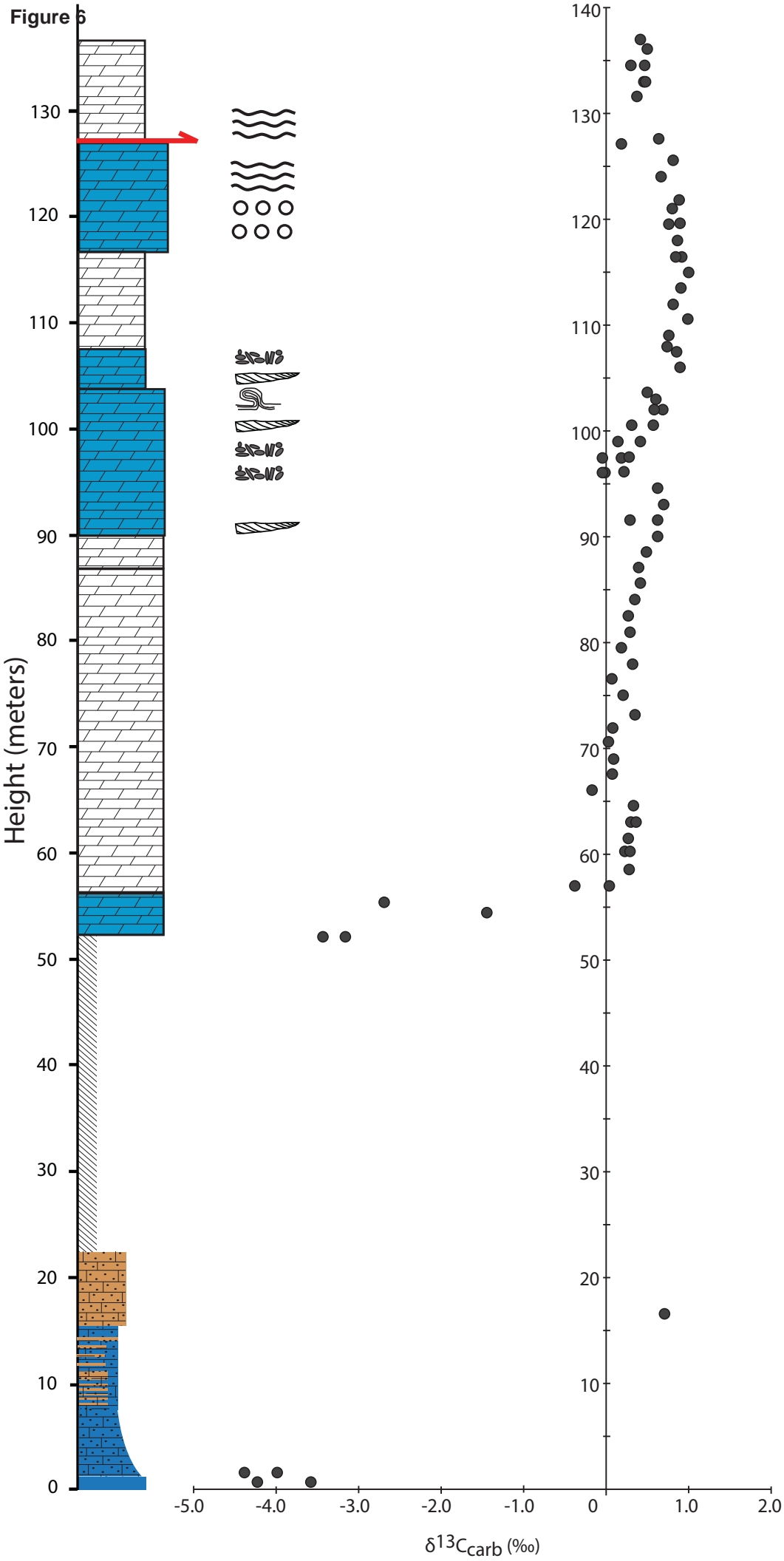


Figure 7
[Click here to download high resolution image](#)

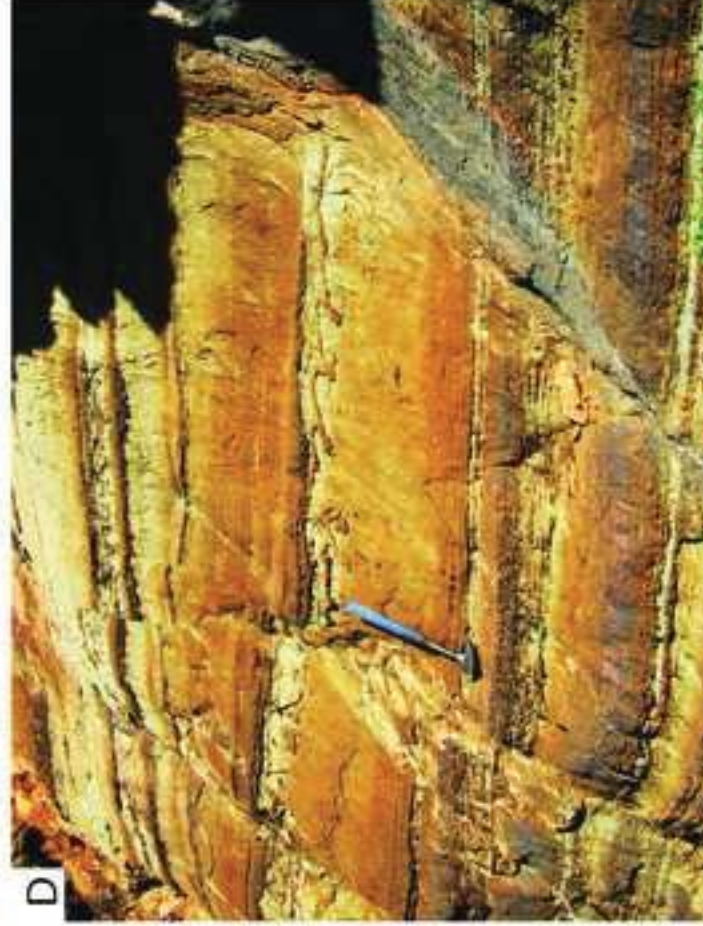
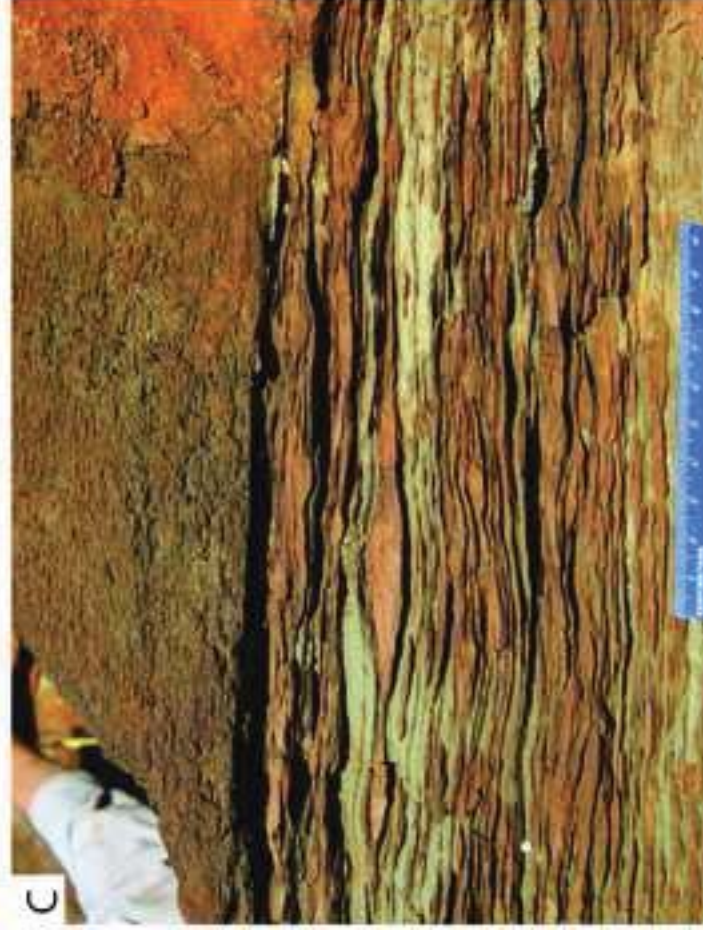
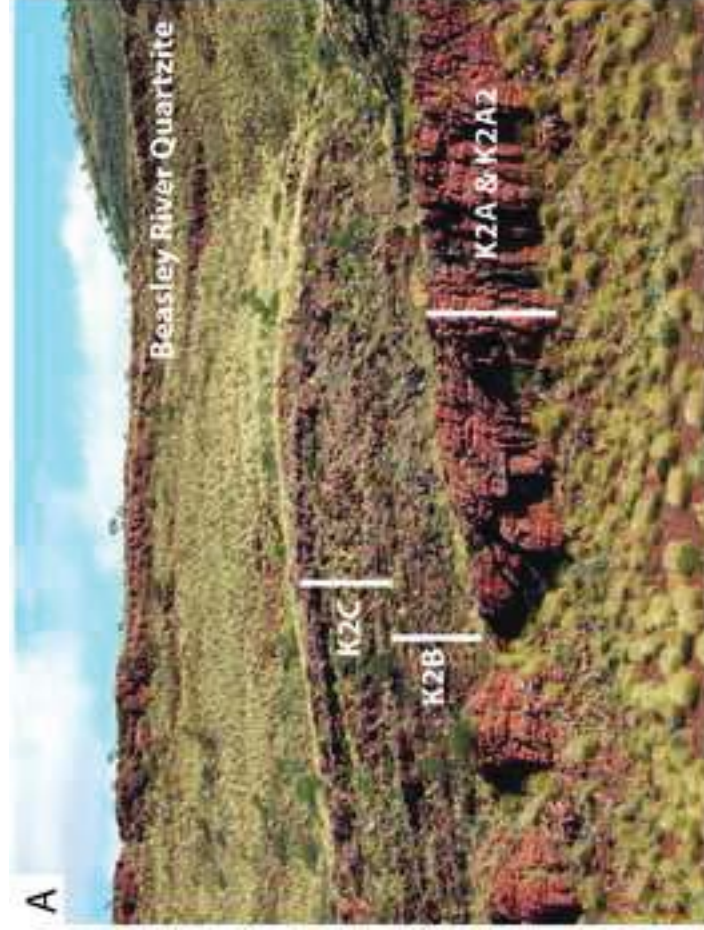


Figure 8

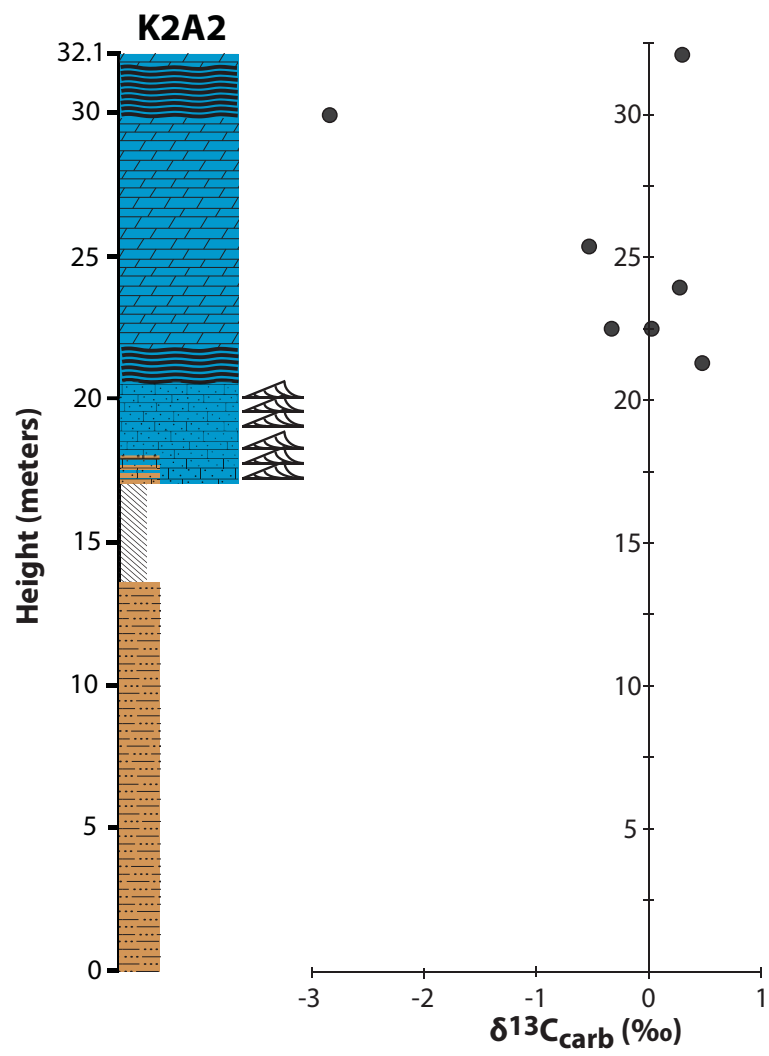
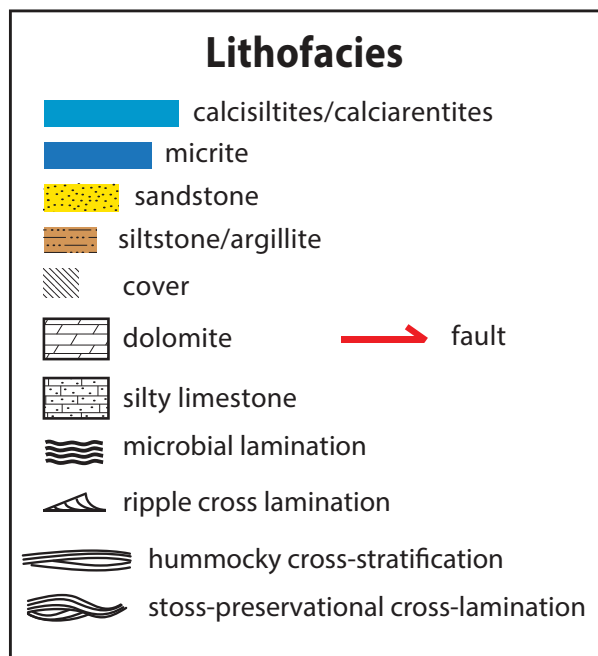
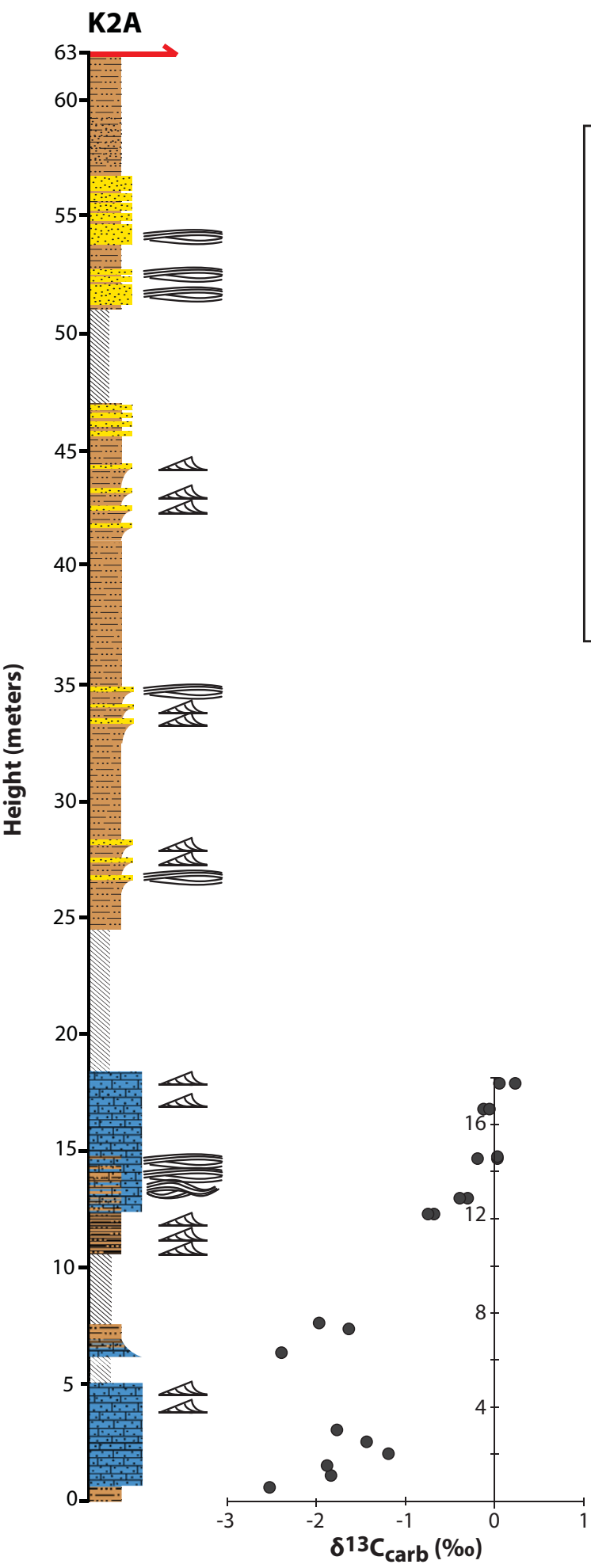


Figure 9

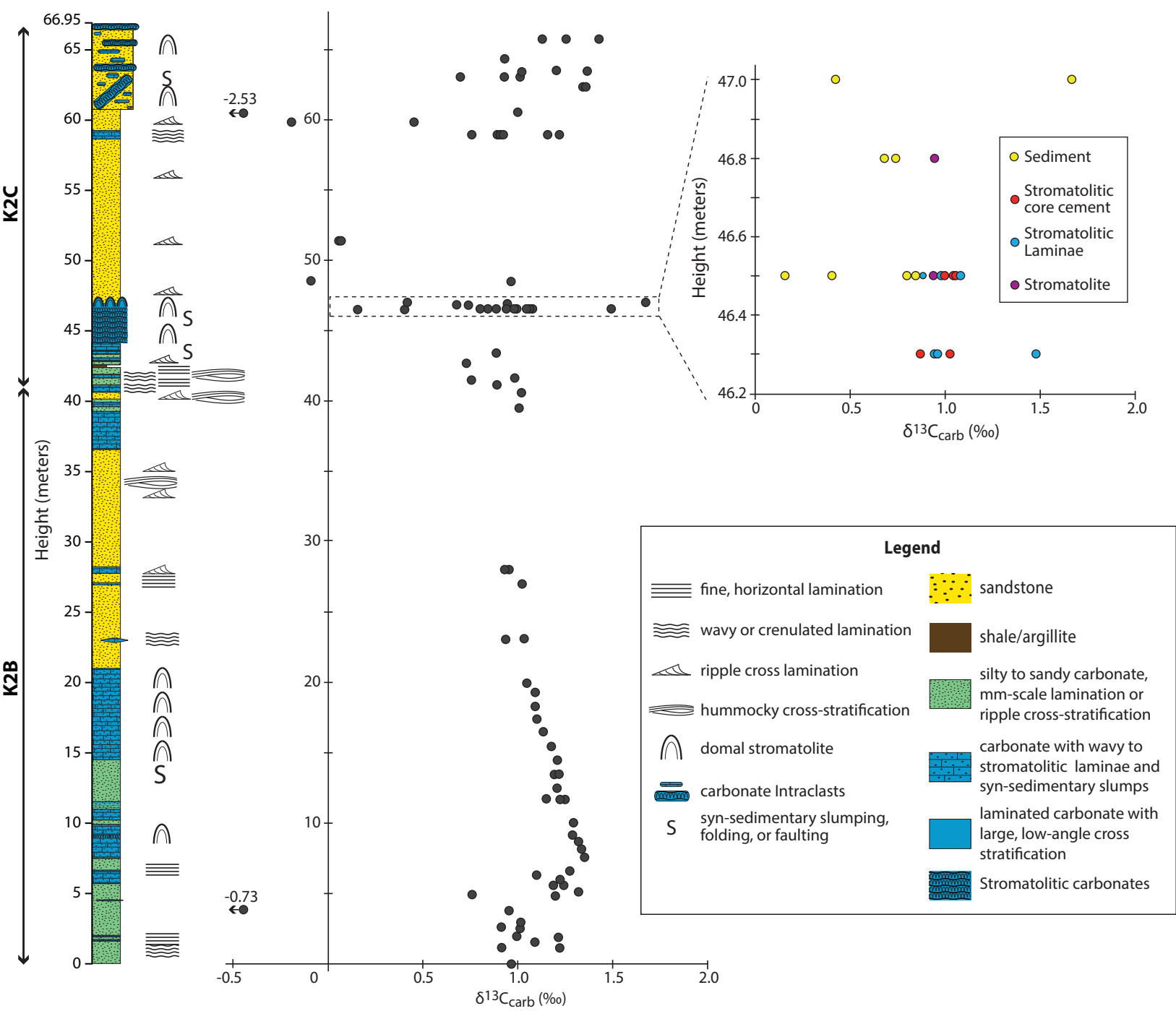


Figure 10
[Click here to download high resolution image](#)

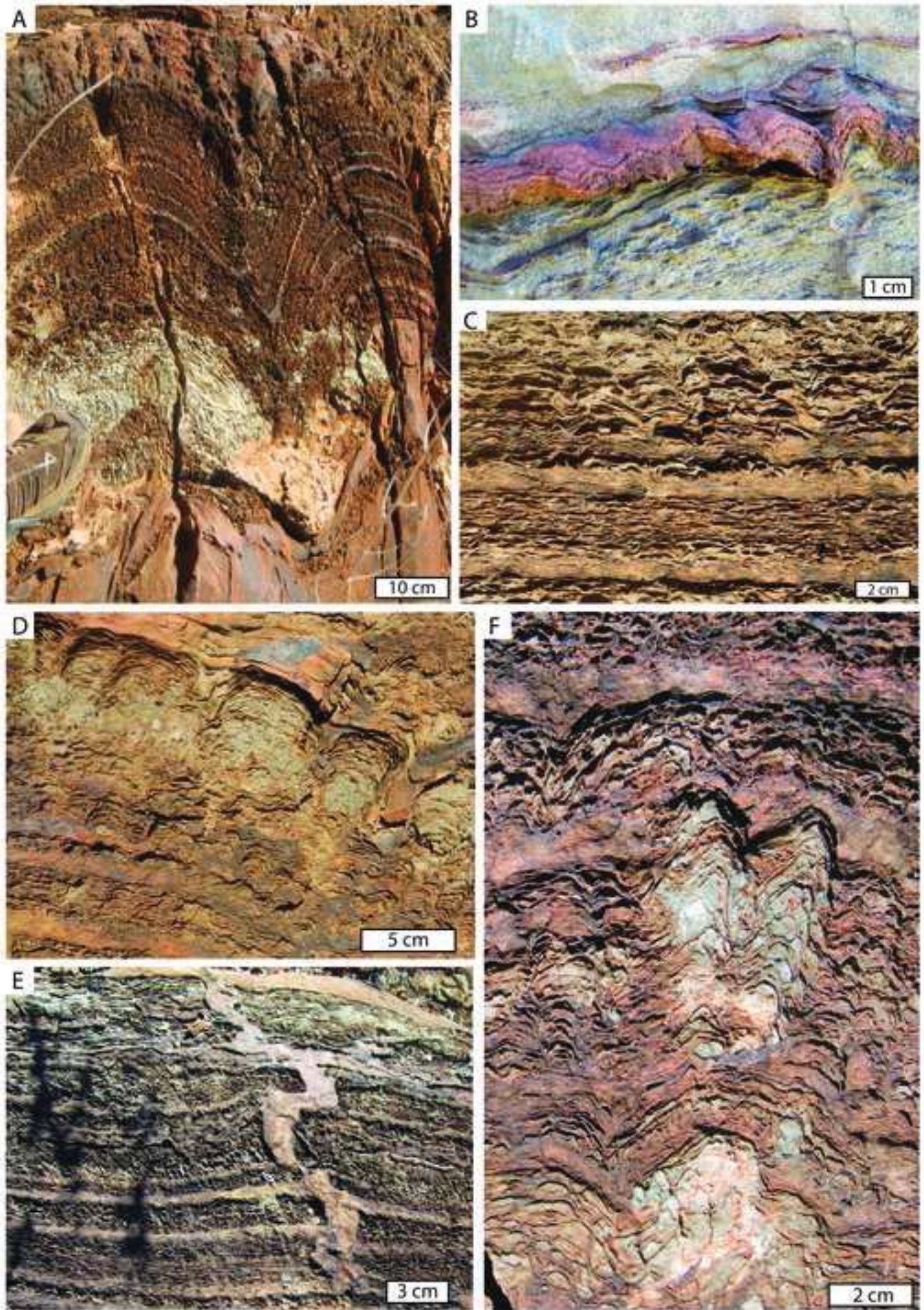


Figure 11
[Click here to download high resolution image](#)

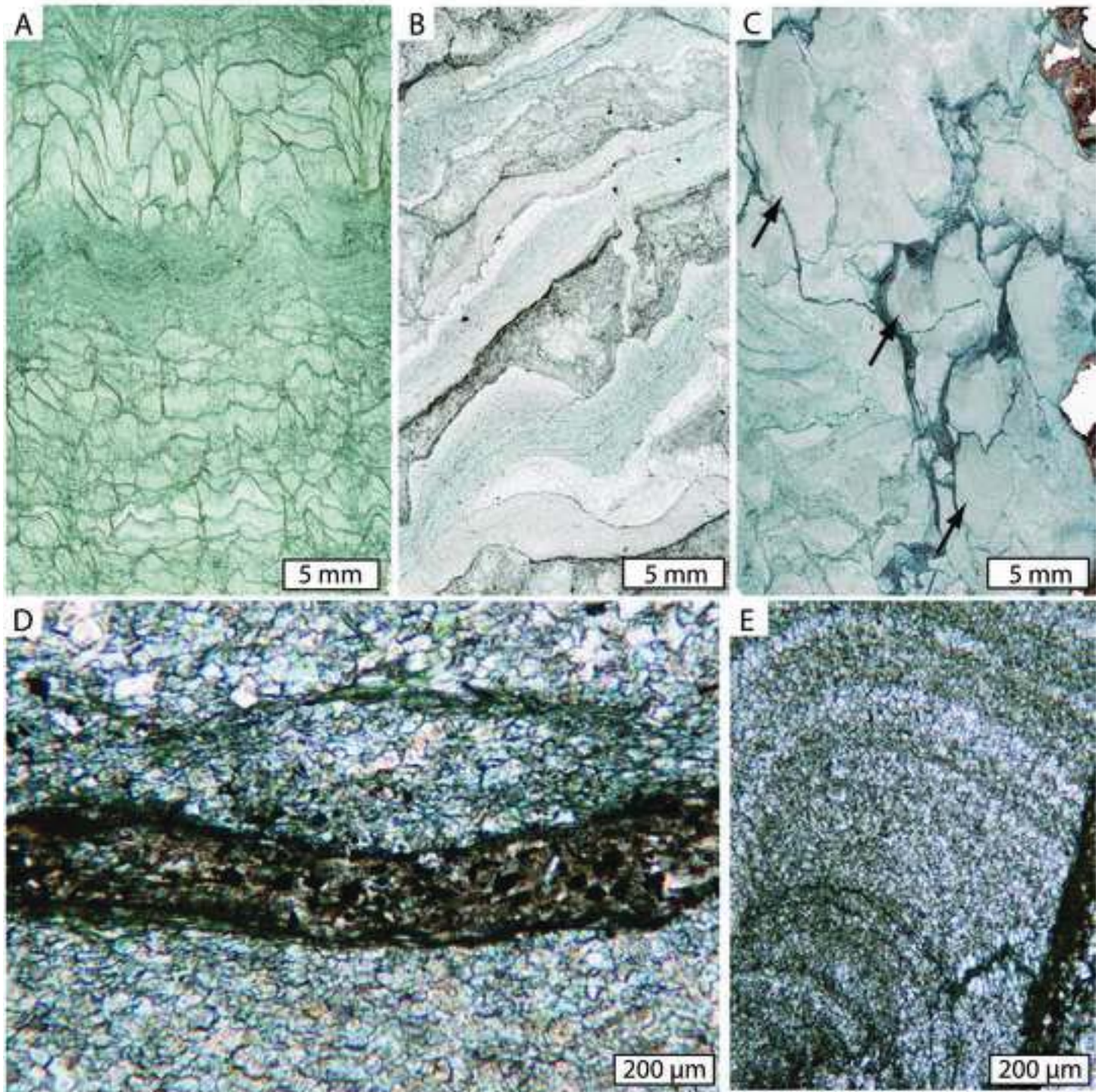


Figure 12

KAZS1 - Kazput carbonate

